Synthesis, characterization and manipulation of Carbon nanotubes

by

Xu Jin

A thesis
presented to the University of Waterloo
in fulfillment of the
thesis requirement for the degree of
Master of Science
in
Chemistry

Waterloo, Ontario, Canada, 2009

I hereby declare that I am the sole author of this thesis. This is a true copy of the thesis, including any required final revisions, as accepted by my examiners.

I understand that my thesis may be made electronically available to the public.

Xu Jin

Abstract

Carbon nanotubes (CNTs) are advanced materials that have numerous novel and useful properties. Controlling the synthesis and properties of CNTs is the major challenge toward their future applications. This thesis addresses this challenge with several contributions.

This thesis begins with the brief introduction of CNTs, including the history of their discovery, their geometric structure, unique properties and potential applications. Then focus is laid on the subsequent three sections: characterization, synthesis, and manipulation of CNTs.

Chapter 2 describes three characterization tools: AFM, SEM and Raman, which are commonly used to analyze CNTs and other nanomaterials. They offer both qualitative and quantitative information on many physical properties including size, morphology, surface texture and roughness. Also, they can be used to determine the structure of CNTS.

Chapter 3 addresses the synthesis of CNTS, because synthesis is an important and indispensible process to study CNTs experimentally. Specifically, two controllable synthesis techniques are realized, which are capable to produce iron catalyst nanoparticles for single-walled carbon nanotube (SWNT) growth. Iron nanoparicles of different sizes obtained from both wet chemistry and electrodeposition can be used for diameter-controlled synthesis of SWNTs.

Following synthesis, two manipulation methods of CNTs are discussed in Chapter 4. Firstly, effort of electrical breakdown of CNTs is introduced. Both SWNTs and MWNTs

(Multi-walled carbon nanotubes) are cut using this method. Moreover, SWNT kink is shown using AFM tip manipulation. These two manipulation methods provide us a possibility to fabricate large cavity from a MWNT for our purposes.

In the end of this thesis, conclusions on my master work in research field of CNTs are drawn and future research directions are proposed.

Acknowledgements

I would like to express my appreciation to my supervisor, Dr.Tang, for the opportunity she granted me to learn more about myself as a researcher, and to build myself as a scientist. I would also like to express my gratitude for her support, patience, and her many constructive criticisms.

I would also like to thank my committee members, Dr. Karanassios and Dr. Anantram for their time spent in both my talks and their many questions regarding my work.

Last but not least, my appreciation goes to all my lab members, and all the friends I made in the Chemistry department.

To my family

Table of Contents

List of Figures

List of Abbreviations

AFM	Atomic force microscope
BSE	Backscattered electrons
CNTs	Carbon nanotubes
CVD	Chemical Vapor Deposition
DI	Digital Instruments
EBPVD	Electron Beam Physical Vapor Deposition
EBSD	Electron back-scattered diffraction
FETs	Field effect transistors
FWNTs	Few-walled carbon nanotubes
HF	Hydrogen fluoride
HRTEM	High resolution transmission electron microscopes
MWNTs	Multi-walled carbon nanotubes
PMMA	Poly methyl methacrylate acrylate
RMS	Root mean square
SEM	Scanning electron microscope
SPM	Scanning probe microscopy
STM	Scanning tunneling microscope
SWNTs	Single-walled carbon nanotubes
TEM	Transmission electron microscope
UV	Ultraviolet
WL	Weak localization

Chapter 1 Introduction

1.1 Discovery of Carbon Nanotubes

As a member of the fullerene structural family, Carbon nanotubes (CNTs) are composed entirely of sp^2 bonds and have a cylindrical structure with high aspect ratio (i.e., length to radius ratio). The unique properties of CNTs have led to valuable applications in electronics, optics, architecture and various other fields.

Most of the academic communities attribute the discovery of MWNTs to Sumio Iijima at NEC in 1991 [1] (cf. Figure 1.1). On the other hand, the major credit for the discovery of SWNTs were given to two different groups, Iijima, *et al.* [2] and Bethune, *et al.* [3], in a scientific point of view, because both groups independently obtained SWNTs by incident while trying to produce transition metal filled MWNTs.

However, the observation of the hollow carbon structure should be traced back to decades ago, particularly, in the fifties after the invention of the transmission electron microscope (TEM). In 1952, the first TEM evidence of nanometer-scale carbon tube was published in the Journal of Physical Chemistry of Russia [4], where Radushkevich and Lukyanovich presented an image of 50 nm diameter multi-walled carbon tubes. However, their work was not noticed due to the Cold War. In 1976, Oberlin, *et al.* showed nano-sized carbon fibers using a vapor growth technique. Their controversial image could possibly suggest a SWNT, even though they did not claim so. In 1979, Abrahamson, *et al.* [5] demonstrated carbon nanotubes produced during an arc discharge at the 14th Biennial Conference of Carbon. Two years later, Soviet scientists presented the chemical and structural characterization of carbon nanotubes created by thermal decomposition of CO.

They claimed that their nanotubes were obtained by rolling graphene sheets into cylinders, and different arrangements (e.g., armchair and chiral tubes) of graphene hexagonal nets are possible [6]. Moreover, in 1987, a U.S. patent was issued to Tennent for the production of "cylindrical discrete carbon fibrils" [7].

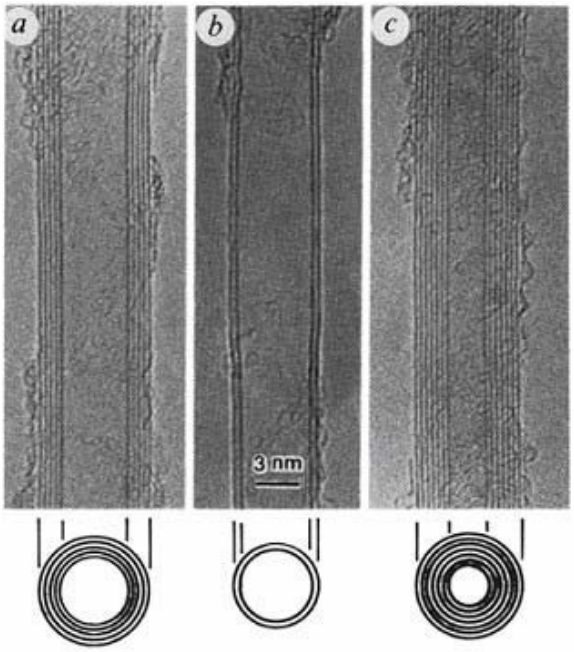

Figure 1.1: The observation by TEM of multi-walled coaxial nanotubes with various inner and outer diameters, D_i and D_o, and numbers of cylindrical shells N reported by Iijima in 1991: (a) N=5, D_o =67 Å; (b) N=2, D_o =55 Å; and (c) N=7, D_i =23 Å, D_o =65 Å. The figure is adapted from ref [1].

Although CNTs have been produced and observed by many research groups in the past, Iijima's discovery of MWNTs [3] is the milestone amongst all. Not only because it was the first clear evidence for the possibility of growing CNTs without catalyst, but also the first time to understand their true nature. Furthermore, after the confirmation of MWNTs using high resolution transmission electron microscopes (HRTEM) on the cathode of a carbon arc, the carbon nanotube research has attracted massive attention and enthusiasm among the

science and engineering communities. Various synthesis techniques and characterization methods have been developed and numerous possible applications have been suggested in the last twenty years.

1.2 Structure of Carbon Nanotubes

To understand the structure and properties of CNTs, the bonding structure of carbon atom in pure carbon should be first discussed. Based upon the hybridization theory, σ bonds in pure carbon can be only formed through sp^2-sp^2 or sp^3-sp^3 hybridized orbital overlapping.

Figure 1.2 presents the structures of graphite and diamond. In diamond, four sp^3 hybridized electrons create four equivalent σ bonds with four other carbon atoms in the tetrahedral directions (cf. Figure 1.2a). This three-dimensional network structure makes diamond the hardest material known so far. The lack of delocalized π bonds suggests that diamond is electrically insulating. In graphite (cf. Figure 1.2b), on the other hand, each atom forms three in-plane σ bonds through sp^2-sp^2 overlapping and one p-p π bond. Even though the bonding within a graphite plane is stronger than that in the diamond, the weak van der Waals interaction between planes makes graphite softer.

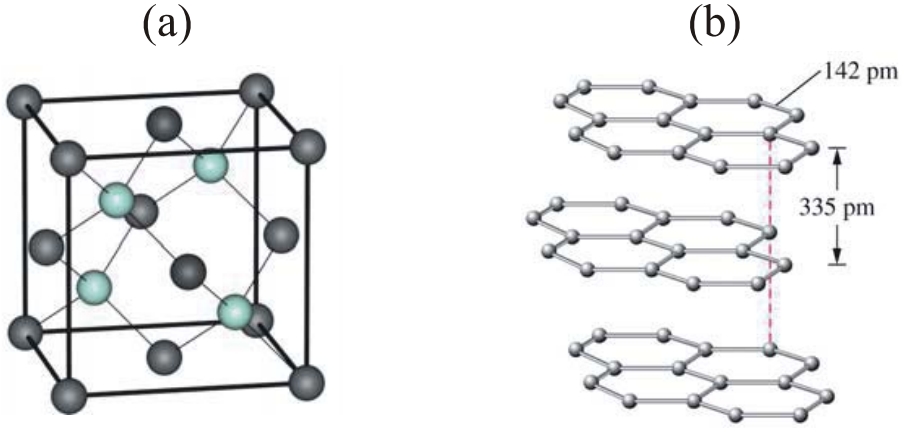

Figure 1.2: Structures of graphite and diamond. The figure is adapted from ref [8]

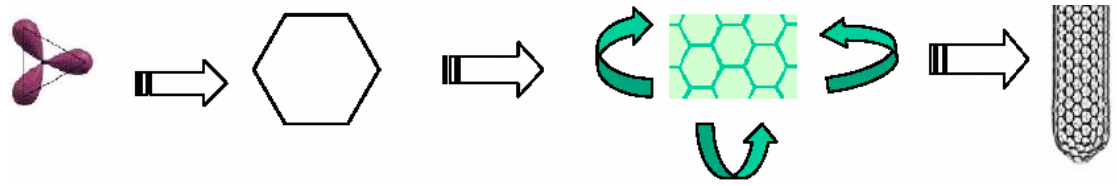

Figure 1.3: Visualization of carbon nanotube formation. The figure is adapted from ref [8].

In a CNT, similar to graphite, a six-fold structure is formed through sp^2 bonding. When more atoms connect together, a honeycomb patterned plane develops. Unlike stacking these layers in graphite, wrapping these layers into cylinders and joining the edges constructs a carbon nanotube (cf. Figure 1.3). Carbon nanotubes are normally categorized as SWNTs and MWNTs depending on shells of graphite. The diameter of SWNTs (cf. Figure 1.4a [9]) ranges from 0.5 nm to 2 nm, while MWNTs (cf. Figure 1.4b [9]) have diameters of 2 nm to ~500 nm depending on the number of layers (e.g., MWNTs with 2-6 layers with a diameter less than 5 nm are classified as few-walled carbon nanotubes (FWNTs)[10]). The spacing between interlayers in a MWNT is approximately 0.34 nm, which has been confirmed by HRTEM [1] and STM [11]. This value, which is close to the distance between graphene layers in graphite, also agrees with the self-consistent electronic structure calculation results [12]. It is also believed that there is little structure correlation between the concentric tubes in a MWNT [1, 13]. In other words, the stacking of carbon nanotubes is turbostratic and the chirality of the tubes varies from layer to layer.

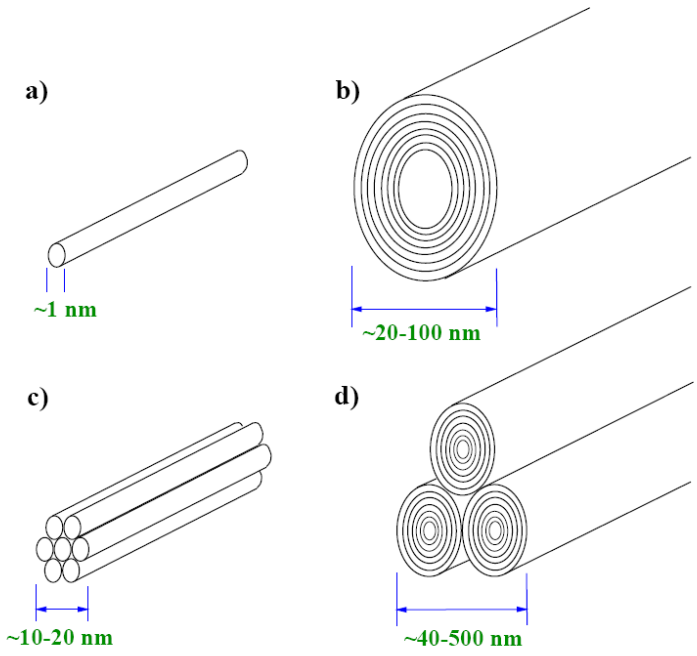

Figure 1.4: (a) an individual SWNT, (b) an individual MWNT, (c) a small bundle or rope of SWNTs, which may have hundreds of tubes, and (d) a bundle of a few MWNTs. The figure is adapted from ref [9].

A SWNT can be characterized by either the chiral angle, θ, or the chiral vector $\vec{C}_h$ (cf. Figure 1.5), given by

$$\vec{C}_h = n\vec{a}_1 + m\vec{a}_2, \qquad (1)$$

where the integer set (n, m) corresponds to numbers of the unit vectors $\vec{a}_1$ and $\vec{a}_2$. As shown in Figure 1.5, the SWNT is denoted as (n, m) tube with diameter

$$D = |\vec{C}_h| / \pi = a(n^2 + nm + m^2)^{1/2} / \pi, \qquad (2)$$

where $a = |\vec{a}_1| = |\vec{a}_2|$ is the lattice constant. The two limiting cases are referred to as armchair tubes ($\theta = 30°$, or $n = m$) and zig-zag tubes ($\theta = 0°$, or $m = 0$), based upon the geometry of the carbon bonds around the circumference of the nanotube. The differences between these two

structures are also shown in Figure 1.6.

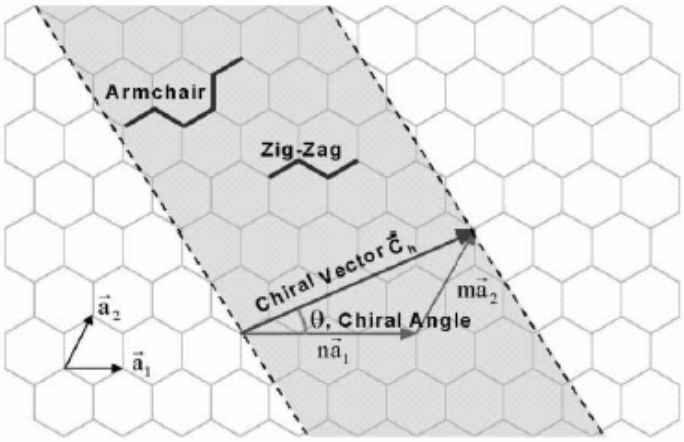

Figure 1.5: Schematic diagram showing how graphite sheet is 'rolled' to form CNT. The figure is adapted from ref [8].

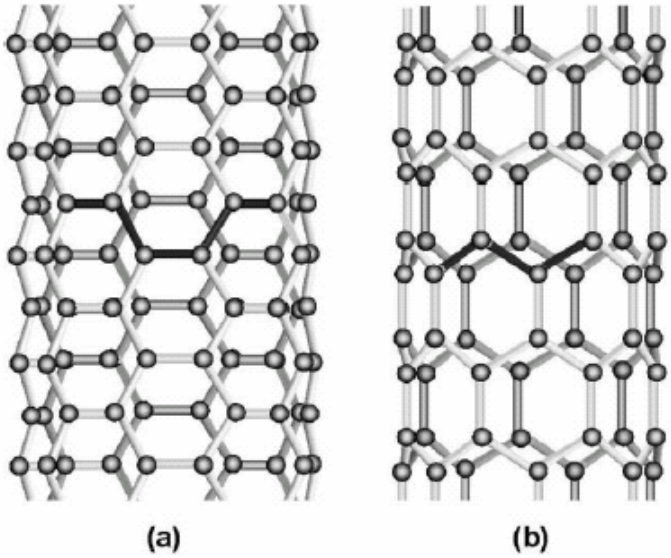

Figure 1.6: Illustrations of the atomic structure (a) an armchair and (b) a zig-zag nanotube. The figure is adapted from ref [8].

1.3 Properties of Carbon Nanotubes

The special structure and chemical bonding of carbon nanotubes provide them unique mechanical, thermal and electrical properties, such as high mechanical strength but low density, high thermal stability and structure dependent conductivity.

1.3.1 Mechanical properties of carbon nanotube

Due to the covalent sp^2-sp^2 σ bonds and the cylindrical structure, carbon nanotubes are one of the strongest and stiffest materials in terms of tensile strength and elastic modulus. In 2000, a SWNT was tested to have a tensile strength of 63 GPa, in comparison to 1.2 GPa for high-carbon steel. [8] Considering their relatively low density (~1.33 g/cm^3), CNTs have the largest specific strength known to man. On the other hand, CNTs also have exceptional high elastic modulus, which is in the order of 1 TPa [8].

CNTs will encounter plastic deformation under extreme tensile strain because of defects formation. This deformation starts at strains of ~5%, which releases strain energy to increase the maximum strain before the tube cracks. Under compression, torsion or bending stress, CNTs tend to buckle because of their hollow structure.

Another interesting property of MWNTs arises from their multiple concentric structures. Since the inner nanotube can slide within its outer shell with little friction, it can serve as perfect linear of rotational bearing. This property has already been used to create the smallest rotational motor in University of California, Berkeley. [11]

1.3.2 Electrical properties of carbon nanotube

The electrical properties of CNTs arise from the graphene electronic structure but highly depend on the nanotube structure, or helicity. In general, an (n, m) nanotube is metallic when $2n + m = 3q$ (where q is an integer), or equivalently $(n - m)/3$ = integer, and a nanotube is semiconducting otherwise. Therefore, armchair nanotubes (i.e., $n = m$) are always metallic, while nanotubes, such as (5, 0), (6, 4), (9, 1) nanotubes, are semiconductors. The resistivity of CNTs is in the range of 10^{-4} to 10^{-3} Ω·cm, while the current density can reach above 10^{9} A/cm^2 [14]. Theoretically, metallic nanotubes can have a current density a thousand times larger than conventional metals (e.g., silver and copper) [14].

1.3.3 Thermal properties of carbon nanotube

CNTs are excellent thermal conductors along the tube axis, undergoing ballistic conduction, but also are good insulators perpendicular to the tube axis. Thermal conductivities of SWNTs and MWNTs have been experimentally determined to be 1750-5800 W/(m·K) and 3000 W/(m·K) respectively. It is also predicted that CNTs will be able to transmit up to 6000 W/(m·K) at room temperature, while copper, a well-known metal with good thermal conductivity, can only transmits 385 W/(m·K).[15] Moreover, the temperature stability of carbon nanotubes has been estimated to be up to 2800°C in the vacuum and 600~750°C in the air.[15]

In conventional metals, electrons are the primary carriers of heat, thus their electrical and thermal conductivity are closely related. In nonmetallic CNTs, however, phonons are the primary heat carriers [16], and the relationship between their thermal and electrical

conductance is still not clear. Since the phonon mean-free-path in CNTs was estimated to be very long (100 nm - 1 μm) [15, 17], some CNTs can have ballistic thermal transport properties [18, 19]. On the other hand, the thermal properties of MWNTs have not been investigated earlier. The ballistic thermal transport is unlikely in MWNTs because of their excessive length (up to 10 μm).

1.3.4 Defects in carbon nanotube

The presence of defects (i.e., incomplete bonding defects, topological defects and chemical defects) will dramatically affect the mechanical, electrical and thermal properties of carbon nanotubes. The mechanical properties of CNTs are affected mainly by two defects. One of the common defects is atomic vacancies, which can weaken the tensile strength of CNTs by up to 85%. Topological defects, or Stone Wales defects, corresponding to the presence of rings other than hexagons (e.g., pentagon and heptagon pairs), will also affect mechanical properties of CNTs. Obviously, the strength of the nanotube will be determined by the weakest segment along the chain.

Defects influence electrical properties of the nanotubes by reducing the conductivity. Thus, metallic tubes can become semiconducting around the defective region. Defects can also lead to phonon scattering, which reduces phonon mean-free-path and consequently reduces the thermal conductivity of carbon nanotubes. It has been predicted by phonon transport simulations that chemical defects (or substitutional defects) only make the high-frequency phonon scattering, while large-scale defects (such as topological defects) lead to the scattering of phonon with diverse frequencies and reduce the thermal conductivity significantly [20].

1.4 Applications of carbon nanotubes

Carbon nanotubes, which offer a wide range of physical, chemical, electronic, optical, thermal and mechanical properties, have drawn enormous attention . For years, their usages have been demonstrated numerous applications among nano-scale electronics, biomedical, composites, structural, and storage.

Due to the high strength/mass ratio, CNTs are used to enforce the mechanical properties of fibers in high-priced sports equipment, such as bicycle frames, golf clubs, tennis rackets, ice hockey sticks and bats for Finland's national sport (called pesäpallo in Finnish). By using CNTs, it is typically achieved to enhance structural polymer (epoxy) composites. Along with their conductivity, the sizes of carbon nanotubes make them an interesting option for the tips of scanning probe instruments, for example the atomic force microscope (AFM) and the scanning tunneling microscope (STM) [21]. Besides, attaching two nanotubes onto a two-electrode AFM tip can make a nanotweezer [23].

Because of the capability of replacing the conventional carbon electrodes, CNTs are testified to have excellent properties for lithium ion batteries [24]. The possibility of using nanotubes as hydrogen storage media has also drawn much attention [21]. Moreover, CNTs can be used as sensors, as the changes of conductance of tube would provide information of molecule attachment. For instance, with nanotube devices, gaseous ambient containing molecules of NO_2, NH_3 and O_2 can be detected with response times an order of magnitude shorter than that for conventional sensors [25].

In addition, CNTs also possess various ideal properties for field emission–based applications: small diameter along with high electrical conductivity and chemical stability.

Based on field emission from nanotubes, prototypes for flat panel displays were already presented in 2001 [26]. Similarly, cathode ray lighting devices have been demonstrated [21]. Besides, semiconducting CNTs can be used as field effect transistors (FETs) [27-30].

CNTs have displayed several interesting transport properties especially at low temperatures [21]. Furthermore, due to their thermal properties, it is practicable to use nanotubes to dissipate heat out from electronic devices. Recently, molecule-filled nanotubes were discovered to behave as thermal rectifiers [22].

Carbon nanotube applications are being investigated in sensing applications, such as biosensors, chemical and pressure sensors. Acting as an ultra sensitive sensor for detecting the hybridisation of target DNA's, NASA has demonstrated MWNT array electrode functionalised with DNA.[31] Recently, chemical sensors have been demonstrated by Surrey University while Rensselaer researchers have demonstrated that a small block of carbon nanotubes can be used as a highly effective pressure sensor.[32]

By filling the hollow core of nanotubes, there are also many possibilities for applications. This structure can be denominated as X@CNT material. As indicated above, successful filling of nanotubes and/or nanoparticles is of great interest in the perspective of applications. In a first step, simple encapsulation has been used to protect nanoparticles from environmental damage. For example, encapsulated nickel nanoparticles were not damaged when stored for several months in aqua region [33]. Nanotubes could thus be used to carry air- or acid-sensitive compounds. In biology or medicine they would also have distinctive advantages in transport of biomaterials and drug delivery. Their potential as a biocompatible electrode for the oxydation of dopamine has been demonstrated [34]. In chemistry, nanotubes could be used as catalyst and catalyst support, as has been realized by deposing ruthenium

clusters for liquid phase cinnamaldehyde hydrogenation on the outer tube surface [34]. Since the inner cavities seem to be less reactive than graphite, nanotubes may serve as nanosized test tubes to carry out chemical reactions inside the cavity [35]. Finally, they have been employed as nanosized moulds, either by using the inner cavity to cast nanowires or by decorating the outer shell. [33].

Other than the above CNTs' properties, however, the toxicity of carbon nanotubes on health and environment has been one of the causes of uncertainties in the development of the market. It is still under debate whether the toxicity exists or not. Nevertheless, the certification of risk management and monitoring by governmental organizations will have a positive impact on the development of carbon nanotubes market. Standardization and codes of conduct are other factors which will assist the development of mass market of carbon nanotubes.

Chapter 2 Characterization of Carbon Nanotubes

In the study of new emerging materials, characterization tools are essential for exploring their basic physical and chemical properties, and therefore revealing potential applications of the materials. To fully depict the structure and properties of carbon nanotubes, a variety of tools will be needed. In this chapter, we demonstrate three characterization methods: (i) atomic force microscope (AFM), (ii) Scanning electron microscope (SEM), and (iii) Raman microscope. In order to clarify the characterization results in later chapters, we will brief the principles, advantages and limitations of these techniques. We also provide examples and details for each tool along with the analysis result as a reference for later researchers in our group.

2.1 Atomic Force Microscope

2.1.1 Brief introduction of AFM

The widespread use of AFM is attributed to the accurate three-dimensional reconstruction of the sample topography with atomic resolution. Meanwhile AFM requires relative low cost and short time period. Another important reason for using AFM is that there is almost no restriction on the sample to be analyzed, unlike SEM in which the sample surface has to be conductive. AFM is typically used in semiconductor studies, biotechnology, life sciences, material sciences, and surface characterizations. In most of the situation, morphological study is the main purpose of using AFM, since it can almost provide real three dimensional

topographic information. Furthermore, AFM data contain important information for structural analysis of the surface as well.

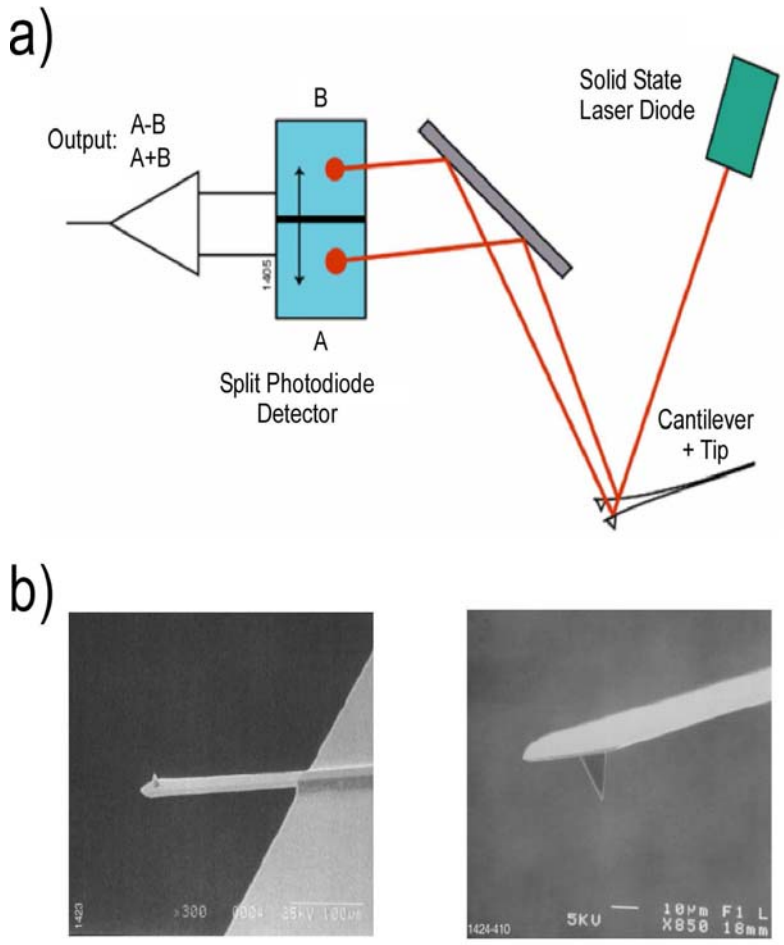

Figure 2.1: (a) Schematic diagram of AFM working principle, (b) image of cantilevers. The figures are adapted from ref [39].

AFM, which belongs to the scanning probe microscopy (SPM) family, was developed by Binning, Quate, and Gerber as in collaboration with IBM and Stanford University in 1986 [36]. Detailed introductions can be found in textbooks and review articles [37, 38]. Figure 2.1a presents a schematic diagram of AFM. The key element of a typical AFM is a silicon cantilever with a sharp tip attached to its end (cf. Figure 2.1b). When the scanning tip is

brought close to the sample surface, there is a force between the tip and the sample that can cause the cantilever to bend. As illustrated in Figure 2.1a, the cantilever displacement can be measured by recording the force-induced detection of a laser beam, where the laser spot reflected by the rear side of the cantilever is monitored by a split photodiode detector. Three different imaging modes could be operated by AFM: contact, non-contact and tapping mode. Only the last mode was used and therefore described in this thesis. In tapping mode, the cantilever is oscillated at or near its resonance frequency. The amplitude of the oscillation will be reduced when the tip contacts the sample surface. By adjusting the tip height, the feedback loop in which a signal can be delivered back to control the system maintains a constant root mean square(RMS) value of the oscillation signal, which is acquired by the split photodiode detector. Therefore, by recording the scanner's vertical position at each (*x, y*) coordinate, a topographic image of the sample surface can be obtained. Since the tip is only intermittently in contact with the sample, the lateral force acting on the sample during scanning is greatly attenuated in comparison with contact mode AFM. This feature of the tapping mode enables one to image individual SWNTs lying on a surface without removing them.

Figure 2.2: A picture of Multimode IIIa Veeco AFM setup in our lab.

2.1.2 Experimental setup

For our research, a commercial Digital Instruments (DI) MultiMode Nanoscope III AFM (c.f. Figure 2.2) was used for the investigation of carbon nanotubes at room temperature. First, the measuring head with the cantilever displacement detection system was installed on the corresponding piezotube scanner. The active vibration isolation table and the acoustic hood were used in order to achieve better vibration isolation between the probe and the substrate during the scanning process. We chose the tapping mode for the topography imaging of carbon nanotubes and small size nanoparticles since the tapping mode shows obvious advantages (i.e., significant smaller tip-sample interaction) in comparison with the contact mode when measuring any poorly fixed object with nanometer size. A dispersant could be used when preparing carbon nanotube samples for AFM imaging. On a silicon wafer,

very dilute dispersant suspensions of carbon nanotubes were spin coated, rinsed thoroughly with water, and then dried in the air before AFM measurement. In general, AFM can measure the diameter of nanotubes. However, due to the fact that different tips have different sharpness, the measurement of nanotube diameter can vary when changing AFM tips. Moreover, AFM still cannot precisely determine the number of shells in nanotubes yet.

2.1.3 Results and discussions

2.1.3.1 Qualitative analysis

Figure 2.3 illustrates two sets of AFM images obtained using Nanoscope(R)III 5.30. Figure 2.3a-c show a series of physical zooming images of a high density coverage of single walled carbon nanotubes on silicon dioxide, where the nanotubes were synthesized by the Chemical Vapor Deposition (CVD) system using iron particles as the catalyst and a combination of methane and ethylene as the carbon source. Figure 2.3d-f present AFM images of gold nanospheres purchased from Sigma-aldrich. The particles were dispersed in deionized water and spin-coated on a 0.25 cm^2 square SiO_2 wafer at 2500 rpm for ten times and ten seconds for each time. The brightness of the image indicates the relative vertical height of the cantilever, and therefore reflects the height of the sample. The zoomed-in image (cf. Figure 2.3c, f) reveals the high resolution feature (1000 times better than the optical diffraction limit) of AFM.

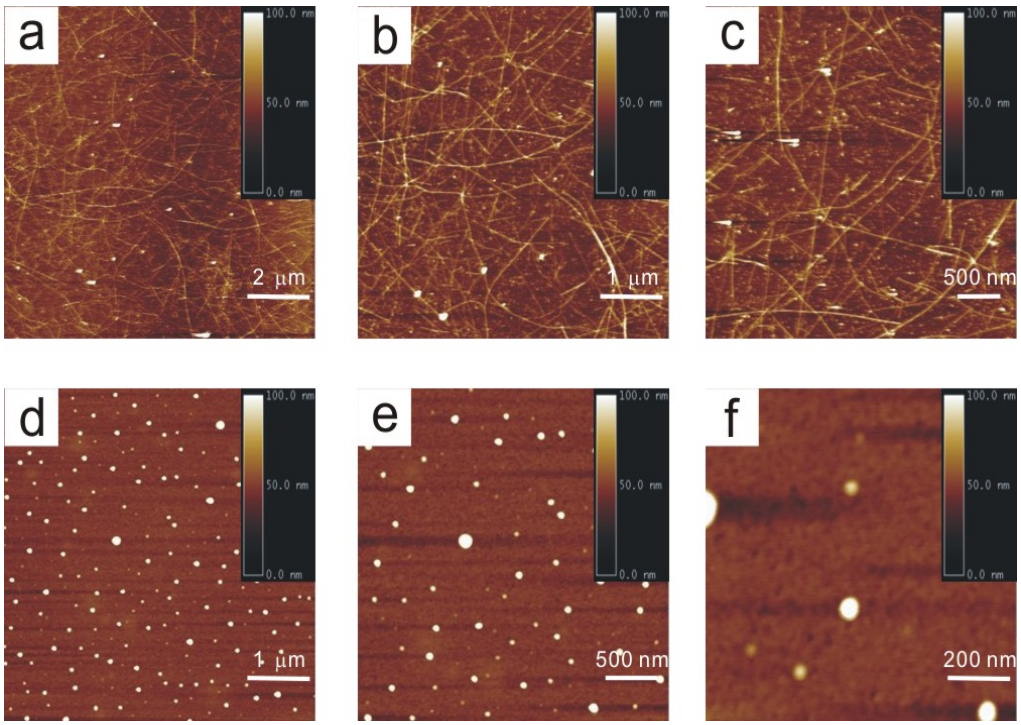

Figure 2.3: AFM image samples of (a-c) single walled carbon nanotubes on silicon dioxide, and (d-f) gold nanospheres. See text for details.

However, the vibration disturbance on the instrument limits the resolution of AFM in the vertical direction (or Z axis), while the diameter of the tip utilized for scanning limits the resolution in the horizontal plate (or X and Y axis). Therefore, the information provided by AFM micrographs is sometimes only relatively reliable.

Qualitatively, AFM can also provide visualization in three dimensions. In Figure 2.4, gold nanospheres are presented in both the top view and the perspective view. Clearly, the bright spots in the top view (c.f. Figure 2.4a) represent the same 3D information as in the perspective view (c.f. Figure 2.4b). However, the latter is more intuitionistic for relative heights of gold particles.

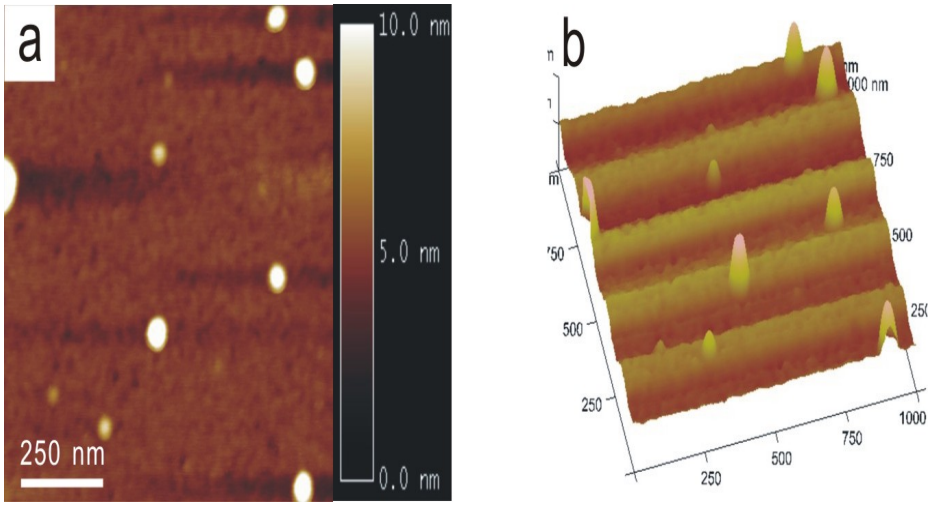

Figure 2.4: AFM images of gold nanospheres in (a) 2-dimension and (b) 3-dimension view.

2.1.3.2 Quantitative analysis

The most important usage of AFM is the quantitative analysis of nano-sized materials, including the size, length, surface roughness, particle counting and size distribution. Figure 2.5 presents examples of various diameter measurements using AFM images, including (a) a multi-walled carbon nanotube deposited on two Pt electrodes, (b) single-walled carbon nanotubes synthesized by CVD system, and (c) iron catalyst nanoparticles obtained from electrodeposition. In each case, a cross section analysis was performed along a representative line. The difference between the vertical readings of the two cursors indicates the particle size or the tube diameter.

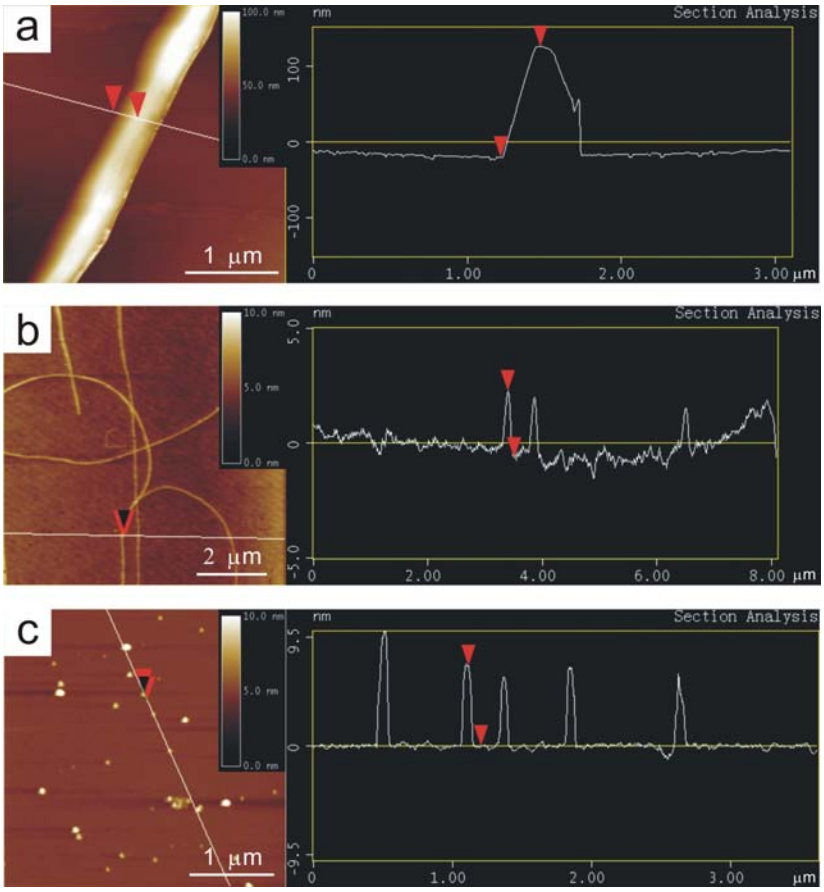

Figure 2.5: AFM images and cross section analysis of (a) a MWNT, (b) SWNTs and (c) nanoparticles. See text for details.

The nanotube length can also be measured using AFM (cf. Figure 2.6). Since a Tapping AFM image is produced by imaging the force of the oscillating contacts of the tip with the sample surface, the relative distance along *z* axis is relative to the oscillation amplitude of the cantilever. By measuring the length of each tube within a sample area of 10µm x 10µm, we obtained a length distribution of oxidized SWNTs in a Osterhout's solution [40]. We found that the solubilized SWNTs were mostly individuals or in small bundles (cf. Figure 2.6a) with length predominately less than 500 nm in Osterbout's solution [40].

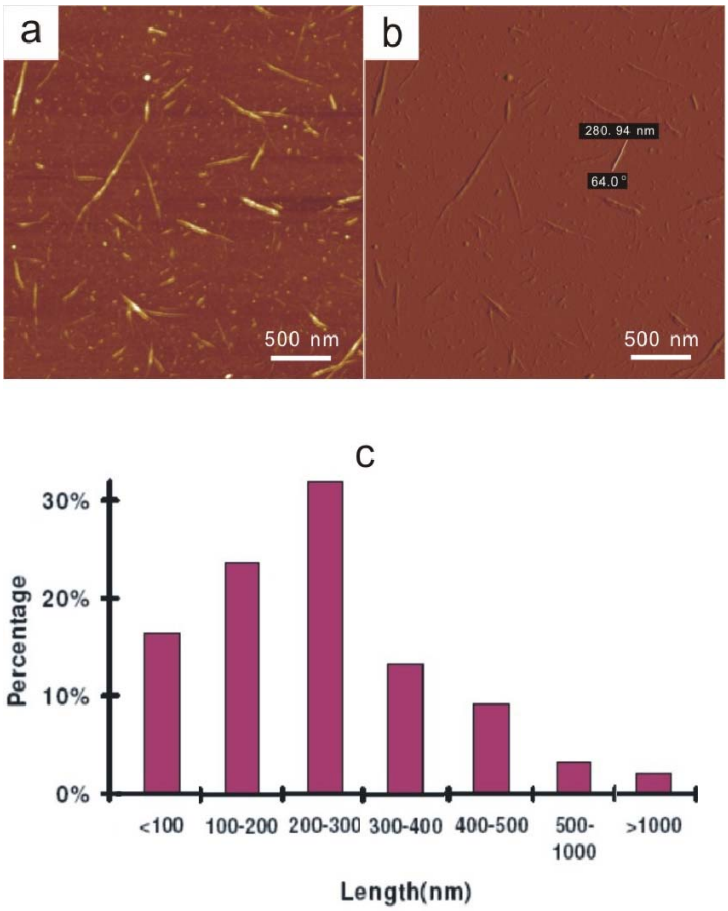

Figure 2.6: AFM images of oxidized SWNTs in a Osterhout's solution, where the z axis is (a) the height and (b) the oscillation amplitude of the cantilever. (c) Nanotube length distribution obtained from (b).

As another example, AFM was used in monitoring the binding via diameter determination between PLO-D4 (the domain 4 of pyolysin) and SWNT-OX(oxidized SWNT). After mixing PLO-D4 and SWNT-OX (10 : 1 ratio) in PBS buffer for 2 hours, the solution was filtered through a MWCO membrane in order to remove PLO-D4 that were loosely bound or unbound. The filter residues were then deposited on a silicon substrate. AFM images for both the residue after binding and the original SWNT-OX are presented in Figure 2.7. The increasing brightness in Figure 2.7b in comparison with in Figure 2.7a indicates the

enlarging size of the sample, and therefore verifies the binding between PLO-D4 and SWNT-OX. Quantitatively, the cross section analysis also shows an increasing height of the sample from 1.367 nm to 6.892 nm because of the binding.

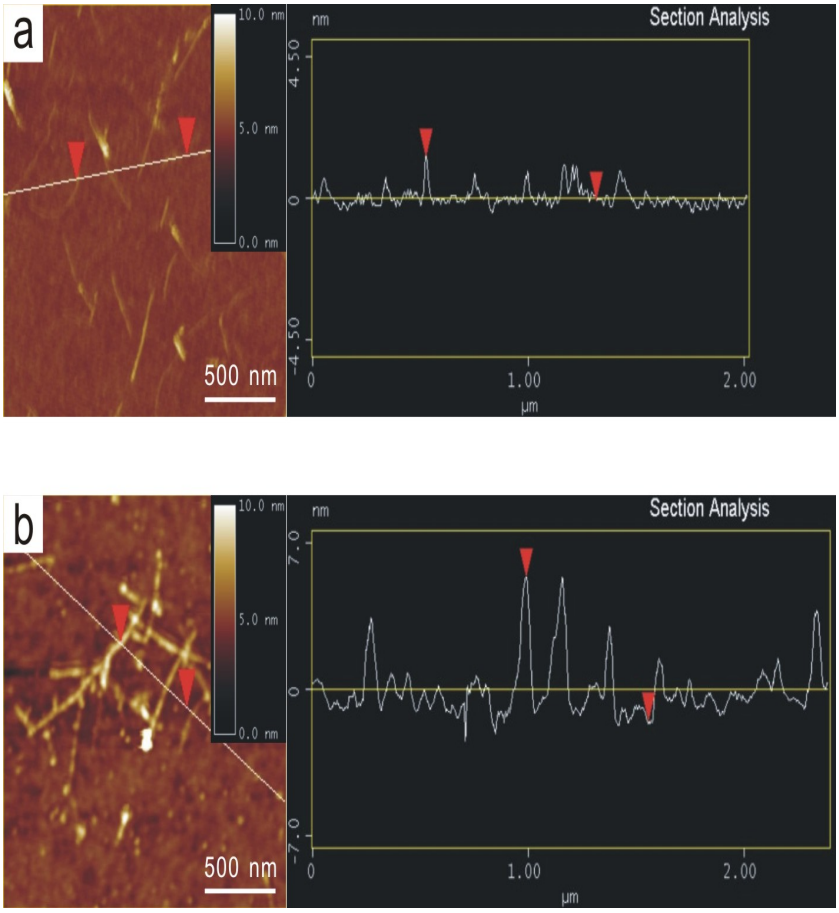

Figure 2.7: AFM images and cross section analysis of SWNT-OX (a) before and (b) after PLO-D4 binding.

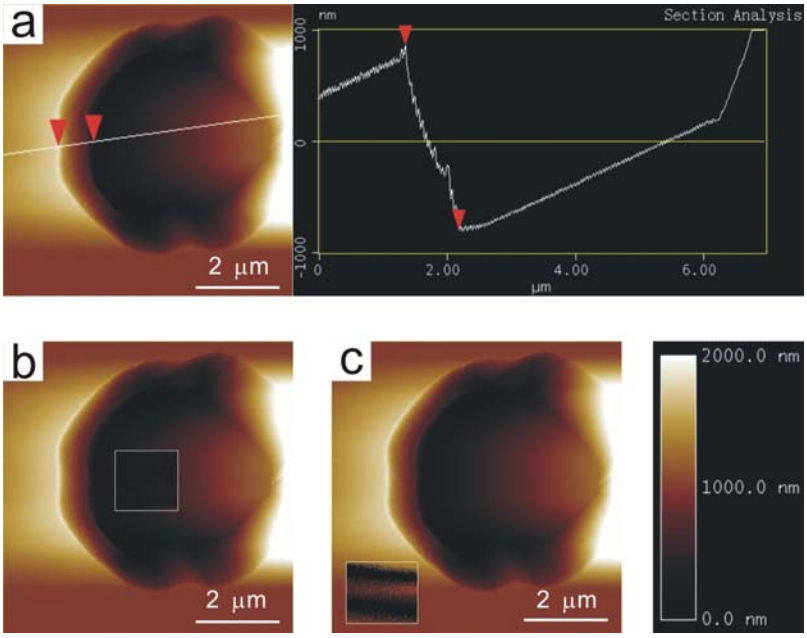

Figure 2.8: AFM images, cross section analysis and roughness analysis of patterned wells for the metal deposition.

Moreover, AFM was also utilized in determining the depth and roughness of surfaces. In Figure 2.8: the patterned well was produced using the UV-photolithography technique (see chapter 4 for details). First, the depth of the photoresist (PMMA) was determined by AFM cross section measurement (cf. Figure 2.8a), and it can help us develop and optimize the deposition condition of the photoresist. Also, the roughness measurement determined that PMMA in the well has been cleaned up after the liftoff process. The mean roughness in the well (cf. Figure 2.8b) is 12.385 nm in comparison to that of 50.875 nm outside. Clearly, the obvious difference in roughness proves that the well surface was clean enough for the next metal deposition step to create catalyst islands for the CNT device fabrication.

2.1.3.3 Conclusion

In conclusion, AFM is a powerful tool for the investigation of the properties of carbon

nanotubes and the development of nanometer sized electronic devices. It offers the capability of 3D visualization and both qualitative and quantitative information on many physical properties including size, morphology, surface texture and roughness. As shown above, statistical information of length, diameter and size can be determined by AFM as well.

2.2 Scanning Electron Microscopy

2.2.1 Brief introduction

With SEM, researchers can view the ropes of SWNTs in a sample or view the highly oriented forest of MWNT films grown on the substrates of quartz or silicon. SEM has a typical resolution limit of about 2 – 5 nm, which might not be good enough to image the individual SWNTs within a SWNT bundle. However, other techniques are available to determine the amount of impurities that often co-exist in the sample (e.g.. amorphous carbon and carbon-coated catalyst particles). Our work on SEM got the help from my coworker, Dr. Himadri Mandal.

In SEM, accelerated electrons carry significant amounts of kinetic energy. When the incident electrons interact with the solid sample, secondary electrons, backscattered electrons (BSE), diffracted backscattered electrons (EBSD), photons, visible light and heat are generated. Secondary electrons and backscattered electrons are generally used to image samples: the former ones are most valuable for showing morphology and topography on samples while the latter ones are worthwhile to illustrate contrasts in composition in multiphase samples (i.e., for rapid phase discrimination). In the sample, inelastic collisions of the incident electrons produce X-rays, with electrons in discrete orbitals (shells) of atoms. As the excited electrons return to lower energy states, X-rays with fixed wavelength (which is

related to the difference in energy levels of electrons in different shells for a given element) are emitted. In addition, SEM analysis is considered as "non-destructive". It is possible to analyze the same materials repeatedly, since X-rays generated by electron interactions do not give rise to volume loss of the sample.

Figure 2.9: A picture of SEM setup in WATlab.

2.2.2 Experimental setup

In our study, a LEO 1530 FE-SEM (cf. Figure 2.9) was used for the characterization of carbon nanotubes and iron nanoparticles. Also, a motorized stage with an attached CCD camera was placed inside a large sample chamber, which allows us to insert and monitor large specimens. With variable pressure limiting apertures, the chamber pressure can be controlled within the range of 1-20 Torr. While gas detection systems are applied to image

the samples, the backscattered electron could be collected using a secondary gas detector through the cascade effect. In order to make it happen, we need to partially ionize the chamber gas to achieve the charge neutralization at the sample surface. The SWNTs were synthesized on a SiO_2/Si substrate and directly mounted on to a standard aluminum mount using the double sided carbon adhesive tape. Further sample preparation or metallization was prohibited in order to capture the natural condition of the fibers. The large field secondary gas detector without pressure limiting apertures is used to image the samples. The above setup allows us to achieve a maximum chamber pressure of 1.5 Torr. Based on the experimental experiences, the best setup to obtain a high-resolution image of carbon nanotubes was determined to be: (a) a working distance of 8-10 mm, (b) an accelerating voltage of 10-30 KV, and (c) a chamber pressure ranging between 0.9 and 1.3 Torr.

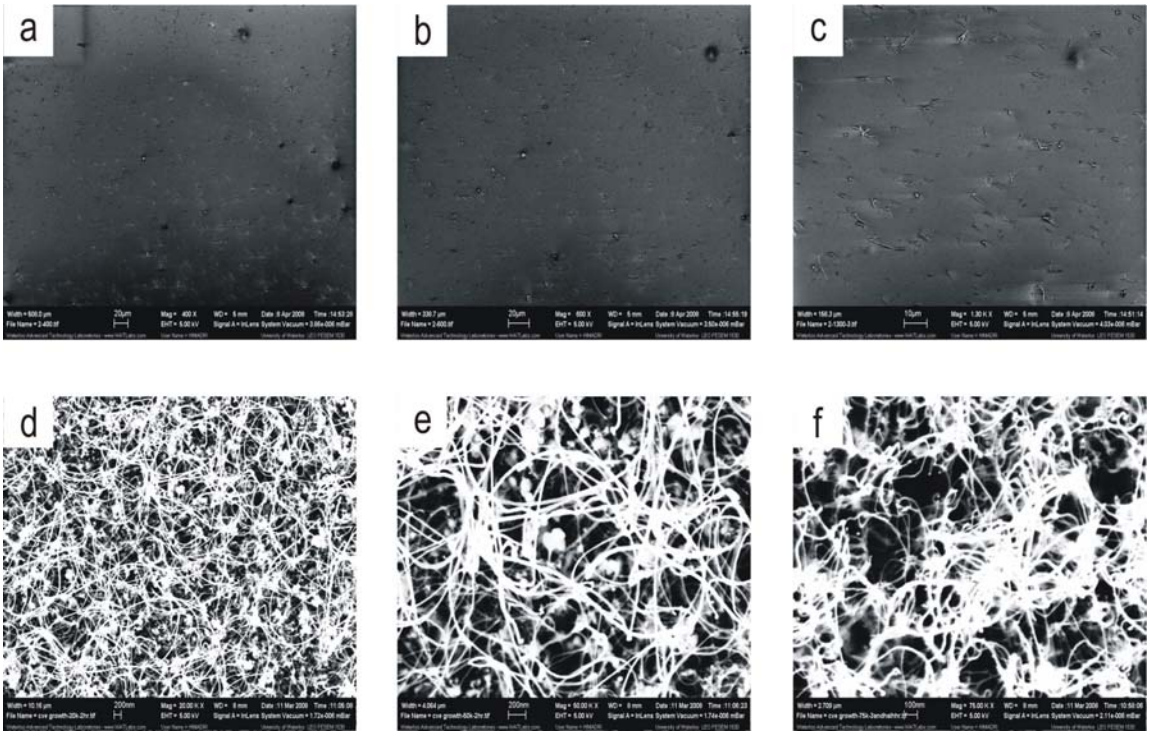

Figure 2.10: SEM images of (a)-(c) MWNTs and (d)-(f) SWNTs. See text for details.

2.2.3 Results and discussions

Figure 2.10 shows two sets of zooming SEM images, where the MWNTs (cf. Figure 2.10a-c) produced by Sigma-Aldrich were dispersed in a dichlorobenzene/ isopropanol (IPA) mixture, and then spin-coated on the Silicon dioxide wafer, while the SWNTs (cf. Figure 2.10d-f) were grown from iron catalyst nanoparticles evaporated by RF sputtering system.

SEM is used as a complement of AFM in most of our study cases; however, there are certain conditions that SEM is the only choice in our lab. Since AFM can only image a maximum height on the order of micrometers and a maximum area of $50\times50\ \mu m^2$ (for AFM in our research lab), it cannot image large scale samples or exceedingly rough surfaces. SEM, on the other hand, is still suitable in millimeter range. Figure 2.11 illustrates samples of SEM images in these cases.

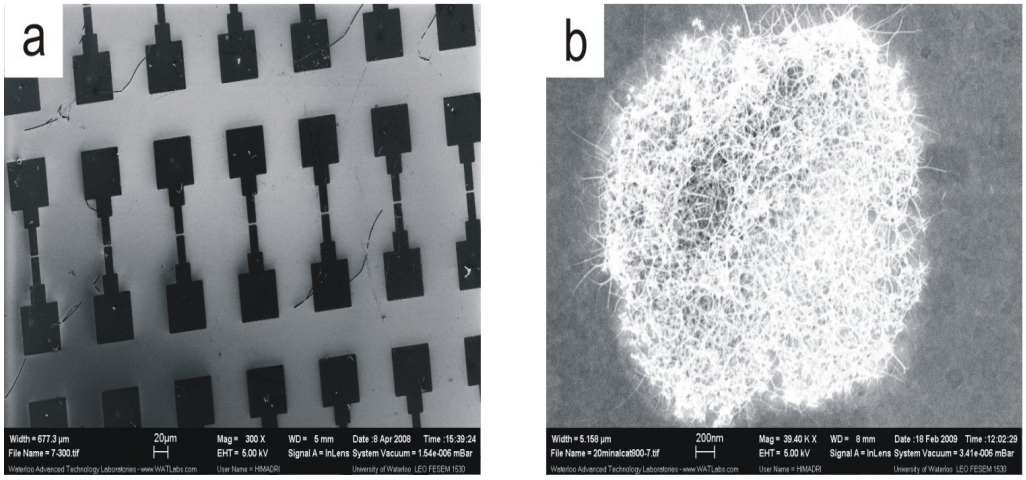

Figure 2.11: SEM images for (a) large scale samples, and (b) rough surface.

Disregarding the specimen size restriction, AFM is still superior to SEM within our research in the following aspects: (a) AFM enables 3-D imaging, while SEM/TEM only

allow images to be measured in 2-D, (b) it allows the measuring of images in all types of environments, such as ambient air, liquids and the vacuum, (c) the overall time required for the whole measurement process, including sample preparation, image capturing and data analysis is much less (often 1 to 4 ratio) than that for SEM, and (d) AFM is more cost effective, space saving and easier to operate.

2.3 Raman Spectroscopy

The third technique involved in this research is Raman spectroscopy. In the last two decades, researchers proved Raman spectroscopy to be a quite useful instrument to detect materials based on carbon element, and it is now adopted widely in related research fields, such as the bonding and properties of pristine, metallic and superconducting materials. This technique has been applied in carbon nanotubes analysis both qualitatively and quantitatively [41]. In this research, however, the Raman spectroscopy was used as an indicator of the appearance of CNTs. All Raman spectra were taken with a LabRam HR system (Horiba Jobin Yvon) equipped with an upright microscope and a piezo sample stage (cf. Figure 2.12).

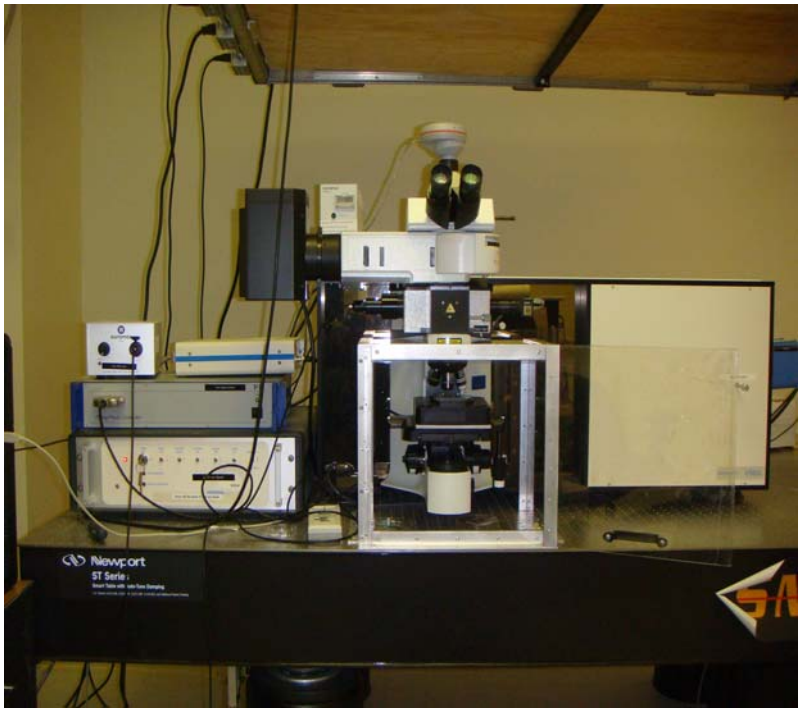

Figure 2.12: A picture of the Raman spectrometer in our lab.

When a beam passes through a chemical compound, a part of the light would scatter in other directions. Even though most of the scattered light remains the original wavelength, some does change due to Raman scattering. The Raman spectra lines depends on the species of chemical molecules, while the detected intensity relies on the number of molecules along the light path, hence also reflects the density of chemical compounds indirectly.

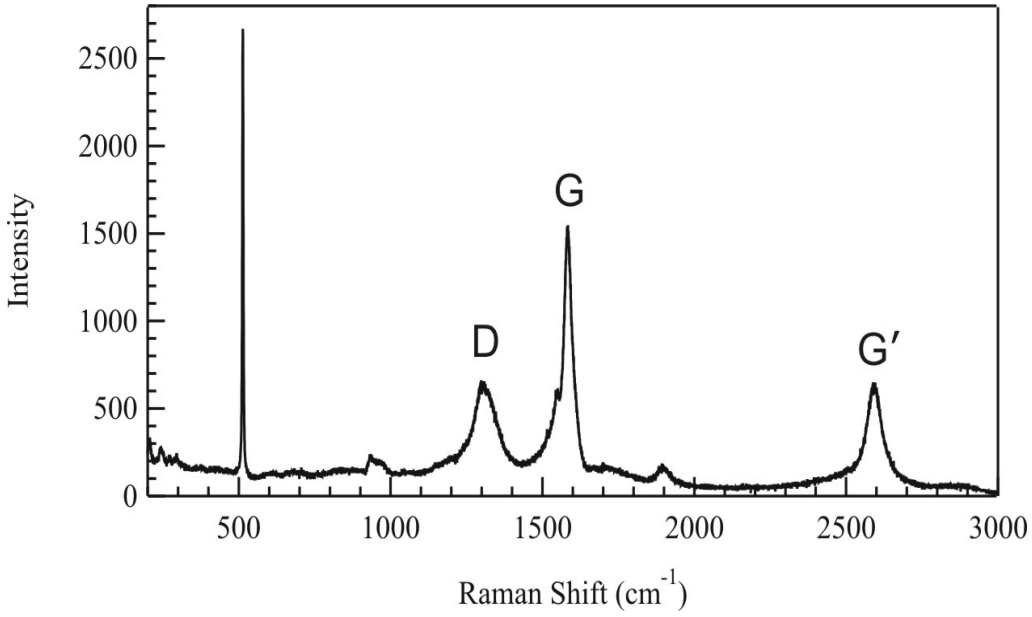

Figure 2.13: The Raman spectrum for a SWNT film synthesized by CVD.

Figure 2.13 presents a typical Raman spectrum for a SWNT. The sharp vibration mode at 1580 cm^{-1} [42], namely the first-order G band, is a result of the presence of sp^2 hybridized carbon domains. Due to the tube curvature, the G band in a SWNT ranges from 1565 to 1590 cm^{-1}. The other major peak, at ~1350 cm^{-1}, represents the disordered sp^2 bonding such as sp^1 and sp^3 carbon, and therefore is called the D (disorder) band [43]. Moreover, the second-order G'-band, at ~ 2610cm^{-1}, is observable for defect-free sp2 carbons.[43] Based on the selection rules, the first-order vibrational mode of the D band should be forbidden in a perfect graphite crystal. However, this band may appear because of decreasing particle size or bending of the lattice fringes. Since MWNTs and amorphous carbon often show strong D band, it is a indication of the defect and impurity level of the SWNT sample, for example, the intensity ratio between the D band and the G' band. The G' band is close to twice the D-band

frequency, and it is an intrinsic property of CNTs and graphite. Therefore, G' band presents even in defect-free CNTs where the D band should be totally absent.

Chapter 3 Controllable Synthesis of Iron Nanoparticles for SWNTs Growth

3.1 Introduction

3.1.1 Synthesis methods

There're mainly three techniques to produce carbon nanotubes: arc discharge, laser ablation, and chemical vapor deposition.

3.1.1.1 Arc discharge

Using arc discharge method to synthesize carbon nanotubes, originally used to produce fullerene, was first introduced by S. Iijima in 1991 [44]. Carbon vapor is formed by arc discharge between two carbon electrodes with catalyst (Figure 3.1) in which carbon nanotubes are able to self assemble. By adjusting the pressure and catalyst carefully, the diameter of SWNTs and MWNTs can be controlled to certain degree.

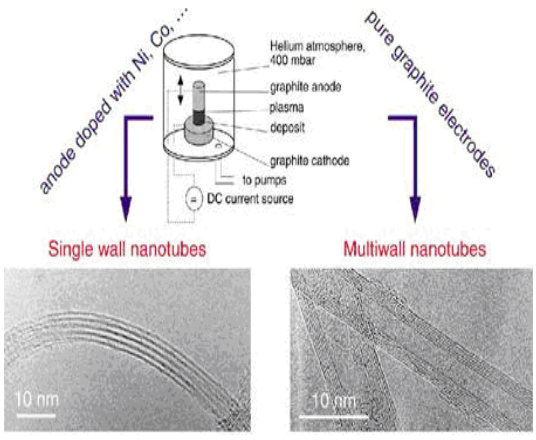

Figure 3.1: Experimental setup of an arc discharge apparatus [1]

The control mechanism on the nanotube growth is partially revealed. The mixtures of helium and argon, with different diffusion coefficients and thermal conductivities, not only influence the diffusion and cooling speed of carbon and catalyst molecules, but also affect the diameter of nanotube in the arc process. This implies that providing appropriate quenching rate in the plasma, single-layer tubules can nucleate and grow on metal particles with different sizes. It also suggests that temperature, carbon and metal catalyst densities can affect the diameter distribution of nanotubes.

3.1.1.2 Laser ablation

In 1995, Smalley's research group at Rice University reported the synthesis of carbon nanotubes by laser vaporization [45]. The laser vaporization apparatus used by Smalley's group is shown in Figure 3.2. A pulsed or continuous laser is used to vaporize a graphite target in an oven at 1200 °C. A very hot vapor plume forms, expands and cools rapidly. The main difference between continuous and pulsed laser is that the pulsed laser demands a much higher light intensity (100 kW/cm^2 compared with 12 kW/cm^2). In order to keep the pressure at 500 Torr, the oven is filled with helium or argon gas.

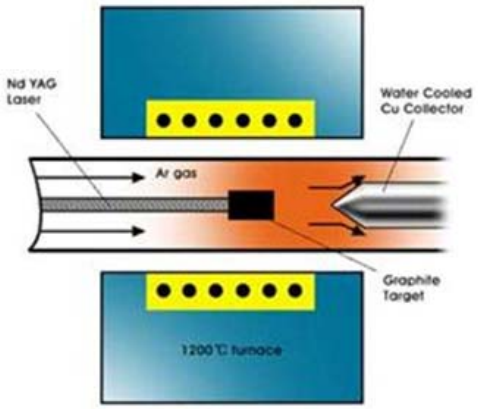

Figure 3.2: Schematic apparatus for laser ablation [45]

Laser ablation is almost similar to arc discharge, because the optimal background gas and catalyst mix are the same as those in the arc discharge process. This implies the reactions probably follow the same mechanism.

3.1.1.3 Chemical Vapor Deposition (CVD)

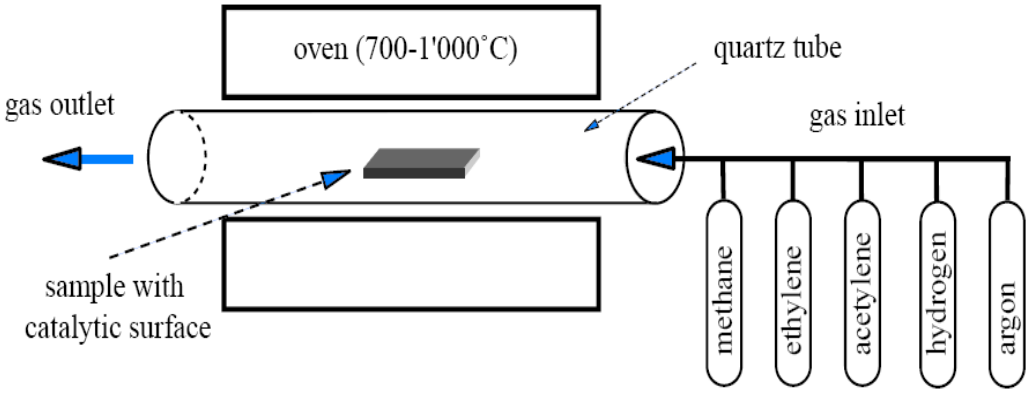

Figure 3.3: Schematic diagram of mechanism of CVD apparatus [46]

Chemical vapor deposition is another widely used method that is suitable to produce on-chip nanotubes directly and hence provides a convenient solution for further device fabrications [46]. The synthesis is achieved by breaking the gaseous carbon molecules, such as methane, carbon monoxide and acetylene, into reactive atomic carbon in a high temperature furnace and sometime assisted by plasma to enhance the generation of atomic carbon [47]. Then the carbon diffuses toward the substrate coated with catalyst particles. Under the correct growth conditions, carbon nanotubes will be formed following the mechanism described before. Essentially, CVD carbon nanotube synthesis is a two-step process. The first step is the preparation of catalyst. Ni, Fe and Co clusters are prevailingly

used catalysts. Catalyst preparation is critical to the nanotube synthesis in the sense that the size of catalyst clusters will determine the diameter of carbon nanotubes. The second step to heat up the substrate in a carbon-rich gaseous environment. Normally, the substrates are put into a quartz tube heated by a furnace to 900 °C with flowing mixed gases of methane and hydrogen. The grown SWNTs have 1~6 nm in diameter and the length can be from several microns to millimeters.

Figure 3.4: The photograph of a typical CVD system in our lab. It has the computer controlled gas flow system, the tube furnace to heat the reaction chamber, and the quartz tube reactor to hold the CVD synthesis.

3.1.2 Growth mechanism

The growth of carbon nanotubes is a catalytic process. Its most likely growing mechanism is assumed to be similar to the one described by Kanzow. [48] In the following section, we will introduce the growth mechanism under lab environment.

With certain experimental conditions, methane is utilized to grow nanotubes with catalyst metal oxide. Methane is thermally stable below 800 ^{o}C without catalyst.

As this reaction: $2Fe_2O_3+3CH_4 \rightarrow 4Fe + 3C + 6H_2O$, metal oxide particles are reduced by methane to pure metal at the beginning. The carbon diffuses into the metal particles remained on the substrate surfaces. After the metal oxide is reduced, the further dissociation of methane is as the reaction: $CH_4 \rightarrow C + 2H_2$. The carbon dissolves and diffuses into the metal particle exothermically with the hydrogen gas removed by gas flow. Once the metal particle is saturated with carbon, some carbon would escape from the less reactive facet of the metal particle, which leads to a carbon density gradient in the particle. This density gradient facilitates more carbon to dissolve and diffuse into the particles. After the carbon leaves the particle, they would assemble in sp^2 structure to avoid the formation of dangling bonds. Then the carbon nanotubes start forming on the less reactive facet of the particle. The schematic representation of the nanotube growth is shown in Figure 3.5: the growth with particles could happen at either the top or the bottom of the nanotubes. They operate under the same principle; even the second is more favored in experiments. The experiment results show that 90% of the nanotubes have closed tips without particles at the top. In the first case, gas (methane) diffuses into the particle from its sides and top. In the second case, the particle adheres to the substrate surface more, and the methane diffuses into the particle from its sides and the nanotube starts growing from bottom up.

At the temperature above 800 ^{o}C, the diameter of the structure becomes larger as the temperature increases. As mentioned earlier, methane is thermally stable without catalyst under 800 ^{o}C; above 800 ^{o}C, it can dissociate spontaneously. Therefore, there are carbon flakes formed by aggregated free carbons in the reaction gas. Meanwhile, the carbon nanotubes with small diameters are constructed catalytically at lower temperature. As the temperature increases, the percentage of the dissociated methane is also increased; more carbon is deposited on the nanotubes which lead to thicker structure. Figure 3.6A showed typical root growth in which no catalyst particles were observed at the tip of the nanotubes. But in Figure 3.6B, some catalyst particles attached to the end of the nanotubes followed by tip growth mechanism.

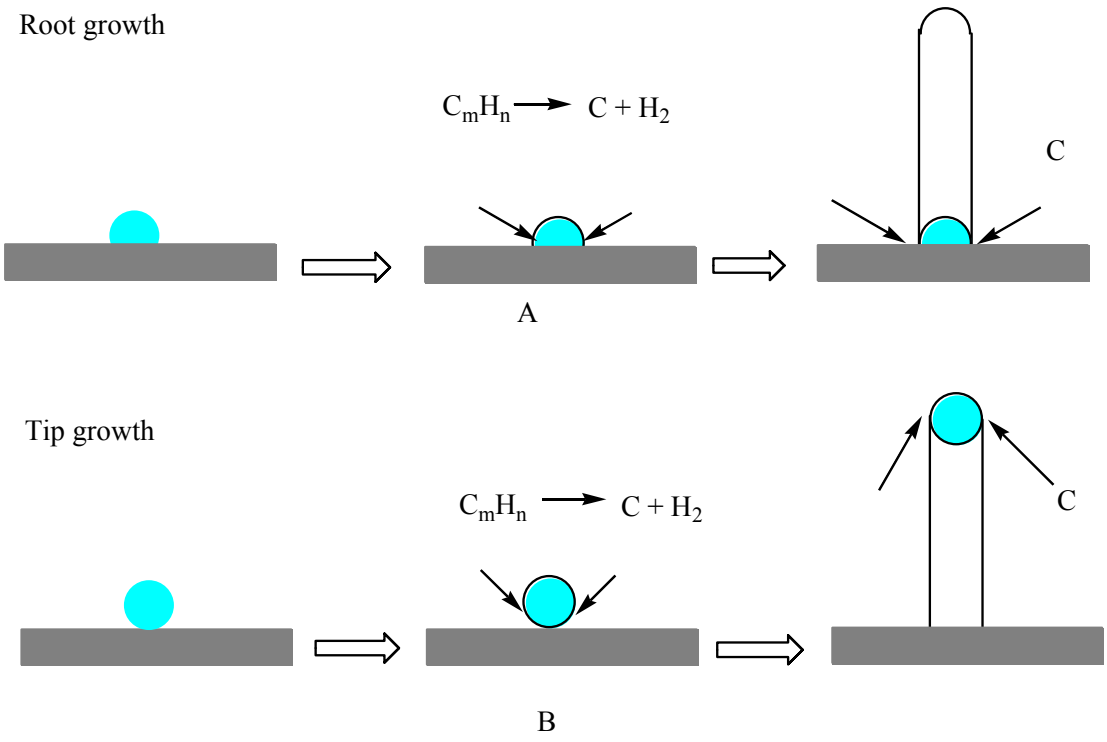

Figure 3.5: Schematic diagram of hypothesis mechanism of catalytic carbon nanotubes growth.

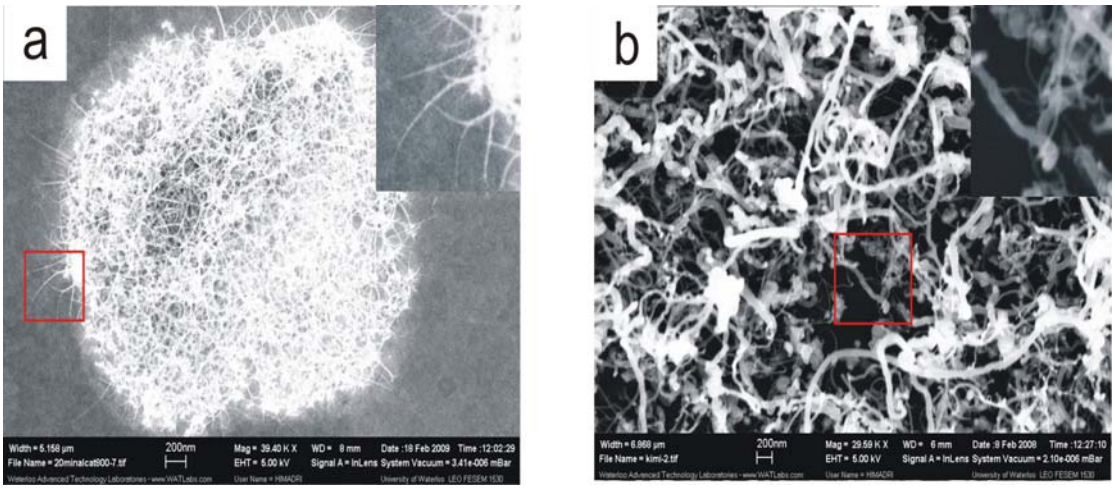

Figure 3.6: SEM images of catalytic grown carbon nanotubes that may due to (a) Root growth and (b) Tip growth.

3.2 Objective

Our objective is to synthesize various sizes of iron catalyst particles for SWNTs with large diameters (around 10 nm). The properties of the nanotubes with large diameters give great potentials for research and applications. [49] Large nanotubes appear to be more stable, as predicted by the energetic argument that the stain energy per carbon is proportional to $1/R^2$ (R is the radium). Their large diameter also gives great encapsulating capacity. Another attractive feature of large nanotubes is their large inter-tube cavities (around 8 nm) in small bundles formed from nanotube aggregation. These inter-tube cavities in the micro-pore range can be accessed by most gas molecules and many organic compounds, even some drug materials. Inter-tube cavities have the equal importance as the nanotubes' inner hollow cavities since they can be used for adsorption investigations and as templates for fabrication of some one-dimensional materials even if all nanotubes are closed. It is believed that these features can bring new ideas on the growth mechanism and new applications, such as nano-

size chemical chest tube or container for organic compounds, biomolecules, and drugs. These features might also provide prototypes to clarify the predictions about the impact of diameter upon their mechanical and physicochemical properties.

3.3 Controllable wet chemistry synthesis of iron nanoparticles

One basic issue in developing nanotube growth methods is the control of nanotube diameter. Previous studies suggested that the diameter of a carbon nanotube is correlated to the size of the growth catalyst in metalized CVD [49]. This hypothesis has been proven by the observation in CVD method that the size of catalytic particles at the ends of nanotubes is commensurate with the nanotube diameters [49-51]. The direct growth of different diameter carbon nanotubes from monodisperse catalysts such as FeO_x, Fe/Mo and Co nanoclusters provided a stronger support for this hypothesis. [50]

We prepared monodisperse iron nanoclusters with three distinct average diameters and used them to grow carbon nanotubes. We expected that the nanotubes with three different diameters should be observed during the experiments.

Additionally, CVD growth showed that in preparation of large diameter nanotubes from large iron nanoclusters, the supply of carbon reactants is critical, and to achieve high quality, the growth temperature and time are also important.

3.3.1 Experimental Section

Thermal decomposition of iron pentacarbonyl was employed in synthesis of iron nanoclusters as the following reaction [51]:

$Fe(CO)_5$ ———Fe-oleic complex+ CO ——FeO/Fe_2O_3

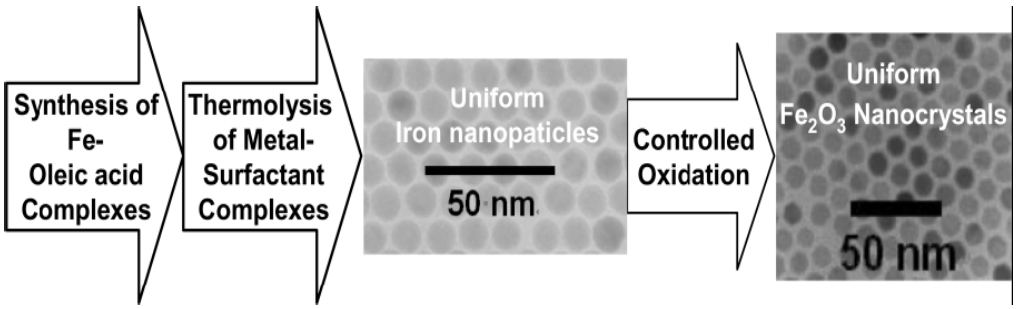

Figure 3.7: Mechanism of the formation of iron monodeiperse nanocluster [51]

At the beginning of reaction, iron-oleid acid complexes formed very quickly. After the thermal decomposition of complexes, iron particles were formed and oxidized to stable ferric oxide particles

All chemicals were purchased from Sigma Aldrich. $Fe(CO)_5$ (1 mmol) was mixed with oleic acid (2-5 mmol) in dioctyl ether (10 mL) and the resultant solution was refluxed under N_2 at 286 °C for 1-3 hrs to yield iron nanocluster solutions with distinct and nearly monodisperse diameters. In this step, particle size was increased by aging at high temperature by catalyst sintering [51]. Following the nucleation, a mild oxidant, trimethylamine oxide ($(CH_3)_3NO$) was added to oxidize iron nanoparticles into Fe_2O_3 nanocrystallites. Then CVD growth of carbon nanotubes was carried out by using iron nanoclusters of different sizes as catalysts and ethylene or methane as the carbon reactant. First, the catalyst was deposited on oxidized silicon from toluene solution and rinsed with hexane; Second, the supported catalyst was then annealed at 900 °C for 5 min in a combination flow of Ar (500 standard cubic centimeters per minute, sccm) and H_2 (500 sccm) as carrier gas; third, methane (1000 sccm) were inserted as carbon source at 900 °C for 10 min. Finally AFM was used to determine the diameters of the iron nanoclusters and carbon nanotubes.

3.3.2 Results and discussions

3.3.2.1 Effect of Protective Agents

In our experiments, oleic acid acted as a protective agent. It is well known that carboxylic groups interact strongly with iron. [52] Long-chain carboxylic acids can be absorbed onto the surface of the metal nanoparticles, forming a dense monolayer and acting as a protective agent. [52]

Long-chain amine (bis-2-ethylhexylamine) was also added as a protective agent in an attempt to produce larger nanoparticles. It was reported that, carbonyl groups in Fe $(CO)_5$ were partially replaced in solutions of nitrogen nucleophiles, forming metal cluster compounds more thermally labile than $Fe(CO)_5$[53]. In addition, mixed acid and amine can form carboxylate anions as following:

$$RCOOH + R_2NH^+ \rightleftharpoons RCOO^- + R_2NH^{2+}$$

It was obvious that the carboxylate anions had a higher electron-donating ability than carboxylic acid. Therefore, they would have a stronger interaction with the nanoparticles and the nanoparticles would be protected more efficiently.

3.3.2.2 Effect of precipitator

A poor solvent such as octane was chosen to precipitate the larger particles. When the poor solvent was added to a mixture containing nanoparticles of various sizes, the biggest particles flocculated first because of their greatest van der Waals attraction. [54]

3.3.2.3 Size control

The synthesis of iron nanoclusters with a narrow diameter distribution is crucial to carbon nanotube growth with controllable diameters. To get a narrow diameter distribution, excess oleic acid (C18) was used in a mixture with $Fe(CO)_5$ as capping ligands for the nanoclusters during the formation. Monodispersed nanoparticles were obtained with the size varying from 5 to 15 nm. AFM images showed that nanoparticles with diameters 5 nm, 11 nm and 15 nm can be achieved by a 1: 2, 1:3, and 1:4 molar ratio of $Fe(CO)_5$ to oleic acid, respectively. To evaluate the ability to control the diameter, diameter distribution was determined based on sizes of 300 particles from AFM images. The following histograms demonstrate relatively narrow diameter distributions (5.2 ± 1.4, 9.7 ± 1.7, and 16.3 ± 2.2 nm).

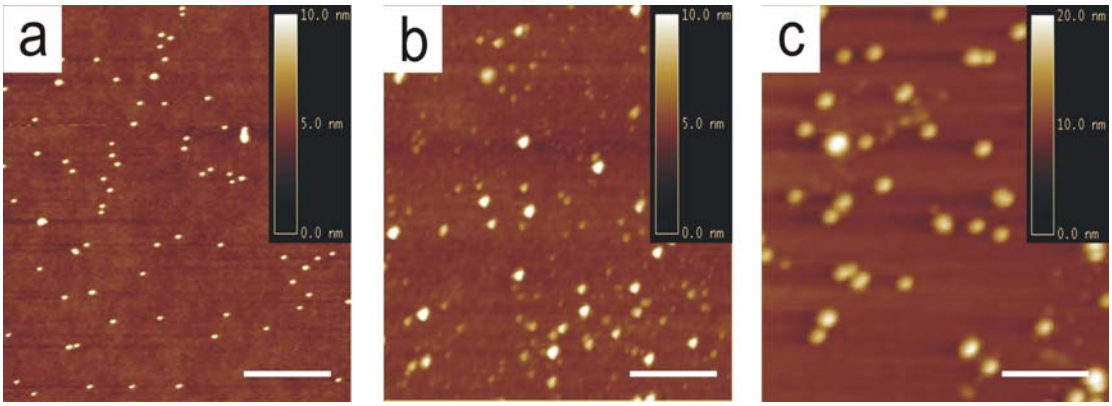

Figure 3.8: AFM images of monodispersed nanoparticles with average diameters of (a) 5.2 nm, (b) 9.7 nm, and (c) 16.3 nm. The scale bar is 200 nm. See text for details.

Further decreasing, $Fe(CO)_5$ relative to oleic acid did not yield larger particles. Therefore, our method was effective in producing iron nanoparticles with diameters less than 15 nm in a controlled fashion.

3.3.2.4 Nanotube Synthesis.

Even though we achieved the goal of controlling the size of catalytic iron nanoparticles, we had some surprising observations from the synthesis of carbon nanotubes: the sizes of the nanotubes did not have an absolute correlation with the sizes of the catalytic nanoparticles under the same growth condition. Most SWNTs have the diameters between 2 to 4 nm regardless of the sizes of the nanoparticles. In our experiments, SWNTs with diameters larger than 5 nm were never observed even iron catalyst particles with 7-15 nm in diameter were applied. For example, Figure 3.9 shows that a 4.1 nm SWNT was synthesized from a 12.2 nm iron catalyst particle. In order to explain this phenomenon, the mechanism of synthesizing carbon nanotubes using iron nanoparticles as catalyst was discussed below:

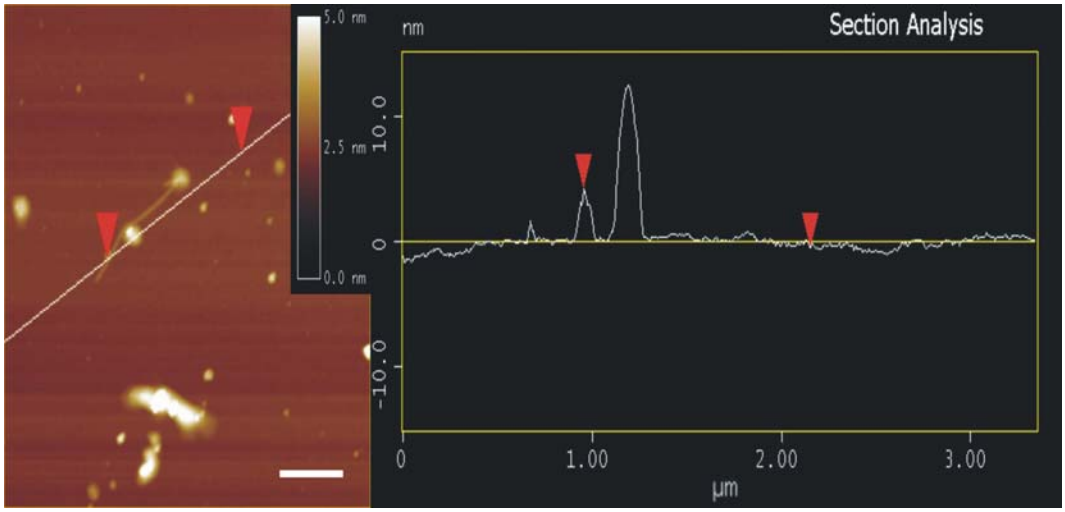

Figure 3.9: AFM images of a SWNT with 4.1 nm diameter grown on a 12.2 nm iron catalyst particle.

Molecular dynamic simulations have been carried out to study the early stages of the growth mechanism in details [55]. The simulation is based on different initial conditions of carbon coverage on iron nanoparticles, including well separated C atoms on free surface of half-passivated iron cluster, where carbons are evenly spaced for simplicity. It is observed

that a fast diffusion of C atoms occurred until the C atoms connect to other carbons Figure 3.10 a.

Short carbon chains are formed through C dimer formation and interconnect to form a grapheme sheet in which all C atoms have sp^2 configuration. Onefold and twofold coordinated C atoms covalently bond to iron atom surface, but threefold coordinated atoms only weakly bond to the surface. The uncoordinated C atoms inside the system bind together and finally are sp^2-bonded. Fivefold and sixfold also appear, as the rings in Figure 3.10 a.

A graphene sheet with sp^2-bonded C atoms will finally form over the iron catalyst surface, with pentagons and hexagons to accommodate the curvature of Fe catalyst surface, as shown in Figure 3.10a. The formed sheet is weakly bound to the Fe surface with oscillation and during the cap formation the C atoms at the edge of the sheet covalently bond to the metallic surface, as shown in Figure 3.10c.

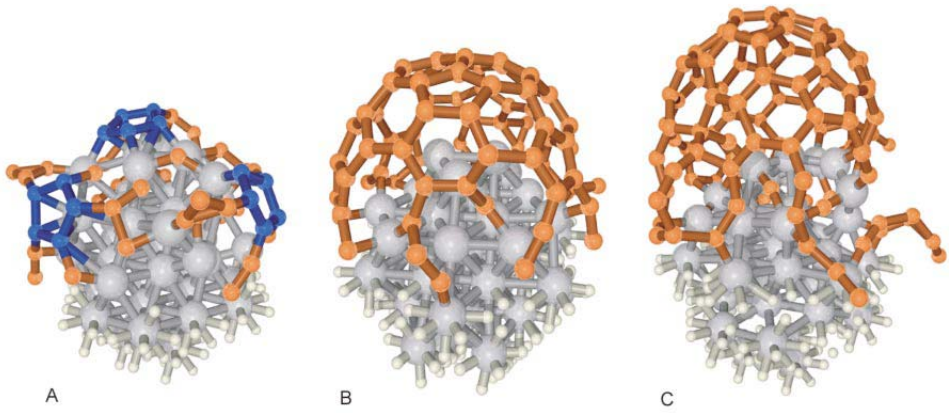

Figure 3.10: (a). Pentagons and hexagons (in blue) of C atoms formed on the surface of 1 nm Fe cluster. (b) and (c). The simulated growth process of a SWNT on surface of a 1 nm Fe cluster.[48]

Three basic steps of SWNTs formation on the surface of Fe nanoparticles are illustrated in Figure 3.11. First, diffusion of single C atom on the Fe cluster surface; second, formation

of sp^2-bonded graphene sheet; third, wall growth by root incorporation of single C atom. This growth process does not depend on the initial C coordination, as the growth proceeds the same way if C dimmers are used instead of single C atoms.

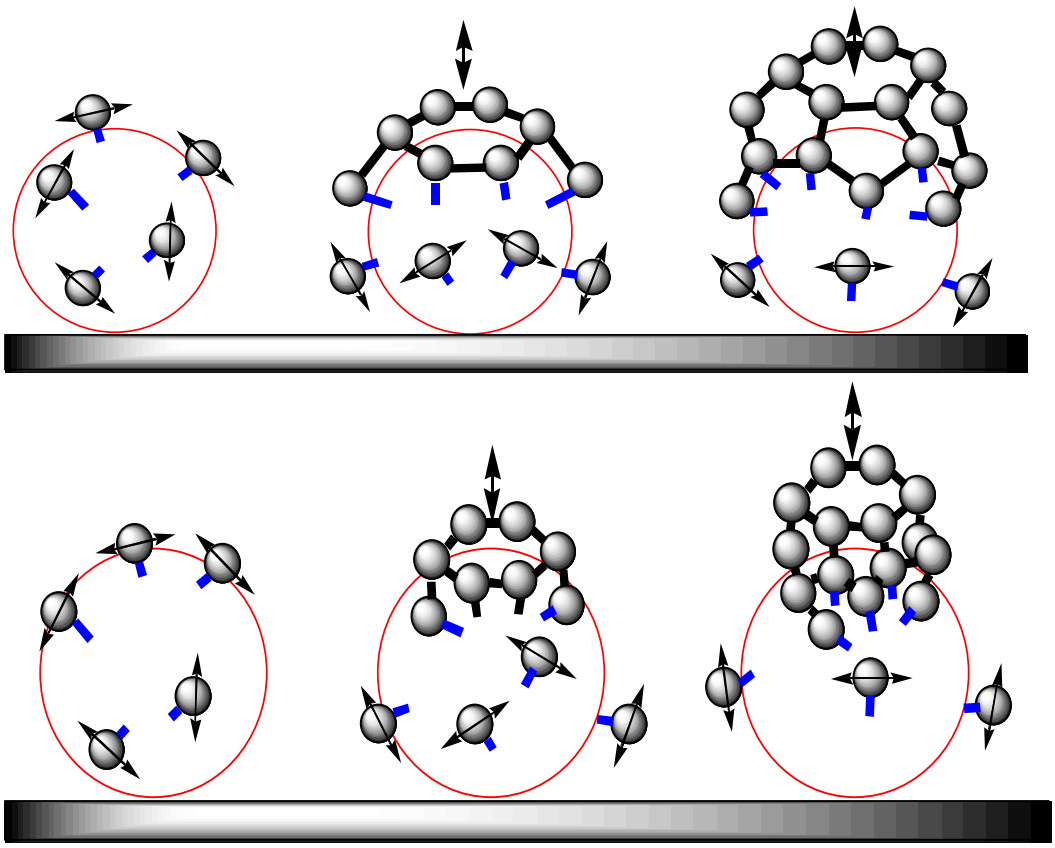

Figure 3.11: Schematic illustration of SWNT growth process on an iron cluster. (a). Diffusion of individual C atom on the surface; (b) Formation of graphene sheet with sp^2-bonded C atoms as a cap on the Fe cluster surface; (c). the growth of wall of SWNT by root incorporation of single C atoms.

Figure 3.11 also shows two possible ways of carbon cap formation. In the first case (Figure 3.11 top), base structure of carbon network happens to cover almost the whole area of particles. Therefore, the size of nanoparticle determines the radius of the nanotube. In the

other case (Figure 3.11 bottom), small carbon cap forms and rises up after the deposition of certain amount of carbon on the small portion of catalyst surface. Harautyunyan et al. [56] also observed that the nanotube diameter was not necessarily correlated with the particle size if the size was larger than 3 nm.

As a result, not only the size and composition of the catalysts are very critical but also the interaction between catalyst particles and carbon source. Although large catalytic particles are prerequisites for growing large carbon nanotubes, efficiency of carbon deposition on catalyst particle is also important for diameter-controlled carbon nanotube growth. Therefore, the parametric studies of CVD growth need to be carried out in order to realize controllable synthesis of SWNTs.

3.3.3 Conclusions and future directions

The study of fundamental properties of nanotubes and exploration of their new applications will be well facilitated by the capability of diameter control to a high degree. For instance, SWNTs with large diameters are excellent systems in studying the electronic properties of radially deformed nanotubes. [57] In addition, they can be applied as electromechanical devices and nanoreactors. [58] Carbon nanotubes with narrow diameter distributions are useful as templates for production of other nanomaterials. [59] Moreover, large diameter SWNTs with large cavities have wonderful structure for future promising applications as we mentioned before.

In this study, size-controlled synthesis of iron particles was realized by Wet chemistry method. Although we did not obtain large diameter SWNTs from lager iron particles, possible explanation and future directions were indicated. Optimizing the growth condition

of SWNTs such as component of carbon source, flow rate of carbon source, growth temperature and growth time will be continued in our lab.

3.4 Electrodeposition of iron particles

3.4.1 Electrodeposition principle

Electrodeposition refers to the process of using electronic current to produce metallic coating on a surface. This process involves putting a negative charge on targeted object immersed in the solution containing salt of the metal that is to be deposited. The metallic ions will be attracted to the target object because they carry positive charge, while the target object carries negative. When they meet, the positive and negative charge will be neutralized and produce metal on the surface of the targeted object. Such process can be elaborated by Figure 3.12.

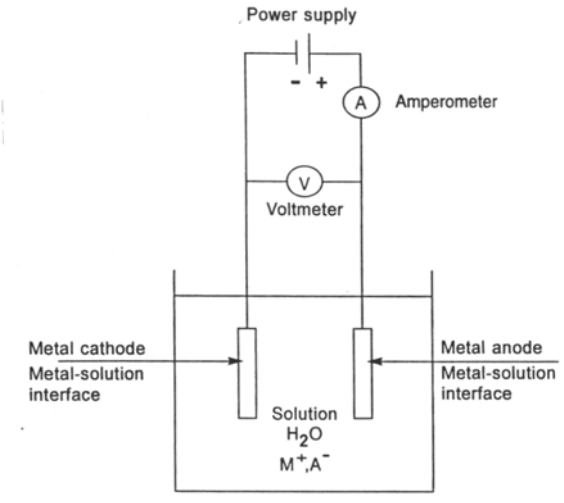

Figure 3.12: Schematic diagram of electrodeposition process

The above section simply illustrates electrodeposition. The same principle was applied in our experiment for controllable electrodeposition of iron nanoparticles. [60, 61]

Before growing carbon nanotubes, the nanoparticles should be synthesized and deposited on the substrate. The nanoparticles can be delivered by chemical vapor, electron beam, or electrochemical deposition. Electrochemical deposition has many advantages over the other two methods: it can carry out enough experiments in a relatively short period of time for a parametric study. The method and experimental parameters affecting the size of nanoparticles will be described shortly.

3.4.2 Experimental methods

3.4.2.1 Hydrogen termination

Before the electrochemical deposition, the silicon surface needs to undergo a process called hydrogen termination. The p-type silicon (100) wafers were washed with a variety of solutions which is shown in this section. Due to the formation of an oxide layer by exposure to oxygen, the wafers were etched up with hydrogen fluoride (HF) at the final step to achieve an atomically flat surface. After the hydrogen termination, the metal particles were deposited electrochemically onto the wafer in a solution bubbled with argon or nitrogen gas. It was observed that hydrogen termination gave more metal deposition and produced a surface with equal reactivity. The deposition was examined using NanoscopeIII AFM and LEO 1530 SEM. The hydrogen termination protocol is shown:

1. Wafers were submerged in HPLC grade acetone and ultrasonicated for ten minutes.
2. Wafers were thoroughly rinsed with millipore water, submerged in isopropyl

alcohol, and ultrasonicated for ten minutes again.

3. Next, wafers were submerged in a 1:1:5 solution of ammonium hydroxide to hydrogen peroxide to water and heated for about ten to fifteen minutes at about 70ºC to 80ºC. This process formed a flat oxide layer and removed any organic material.
4. Wafers were then rinsed again thoroughly in millipore water and submerged in a 1:1:5 solution of concentrated hydrogen chloride to hydrogen peroxide to water for about fifteen minutes. This helped to remove any inorganic wastes.
5. After rinsing each wafer (one by one) thoroughly again with millipore water, the wafers were submerged in 2% hydrogen fluoride for about 30 minutes.
6. Finally, wafers were rinsed three to four times with Millipore water and put in a nitrogen box for drying.

In our experiments, the hydrogen-terminated wafers were used within 24 hours.

3.4.2.2 Solution preparation

The deposition was done in electrolyte solution (10mM $FeCl_2.4H_2O$, 0.1M H_3BO_3). Fe (II) solution was unstable and very easily oxidized in air. Therefore the solution must be freshly prepared prior to use by dissolving $FeCl_2.4H_2O$ in stock H_3BO_3 solution. The solution was bubbled with N_2 gas for 20 minutes to get rid of some of the dissolved oxygen before the deposition.

3.4.2.3 Deposition setup

The electrodeposition was carried out in a cell system consisting three electrodes: reference electrode (Ag/AgCl), counter electrode (platinum), and working electrode (Figure 3.13). The hydrogen-terminated silicon (100) wafer was screwed in the working electrode as cathode, while the counter electrode as the anode.

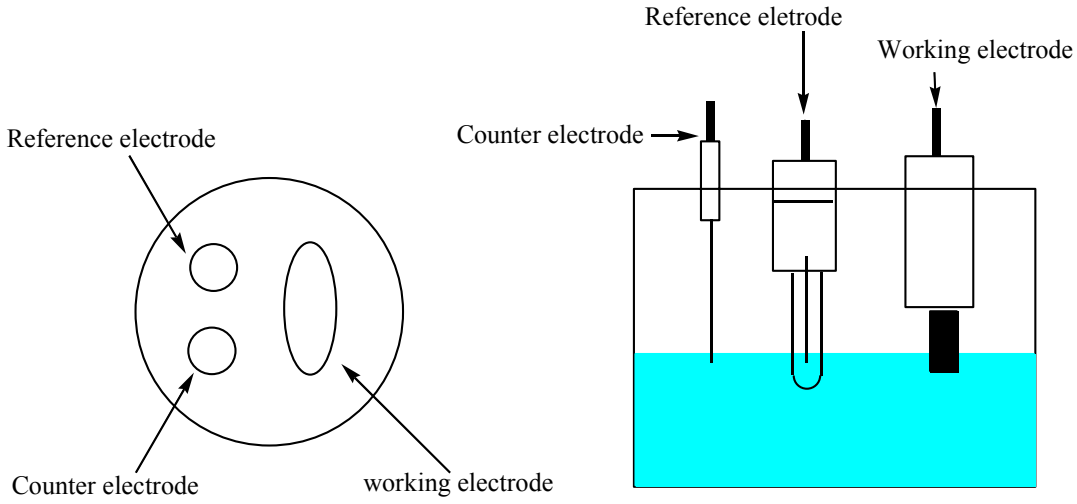

Figure 3.13: Three-Electrode Cell Experiment Setup in Watlab. A H-terminated Si wafer is screwed in the working electrode and an O-ring is used along with the support shown on the side to hang the electrodes into solution.

A CH instruments 660 A electrochemical workstation was used. The two most common deposition methods used are cyclic voltammetry and amperometry. In cyclic voltammetric method, a selected range of voltages is applied at a certain speed (V/s) for a selected number of sweeps, that one sweep is equivalent to a linear sweep voltammetry experiment. Cyclic voltammtry can quickly identify the reduction and oxidation peaks for the metal when the voltage range is outside of the hydrolysis of water. It gives a current versus voltage graph. In amperometric method, a constant voltage is applied for a fixed period of time or amount of

charge. It gives a current versus time graph. We used amperometric method in our experiments.

3.4.2.4 AFM and SEM characterization

AFM and SEM were used for the direct observation of the morphology, size, and any interspatial arrangements of iron nanoparticles deposited on the silicon wafer.

3.4.3 Parametric study and results

By manipulating the experimental parameters, such as the solution concentration, the deposited charge, and the applied potential, the iron nanoparticles behaviour and optimal deposition condition could be determined

3.4.3.1 Dependence of solution aging

The iron nanoparticles were deposited from the $FeCl_2 \cdot 4H_2O$ solution. As mentioned earlier, this solution was very unstable; the ferrous ions were easily oxidized to ferric ions with the color of solution changing from clear to yellow-orange color. The age of the solution had a great impact on the iron (III) nanoparticles deposition. It resulted in rod shaped particles with uniform size if the solution aged for 7 days after deposition.

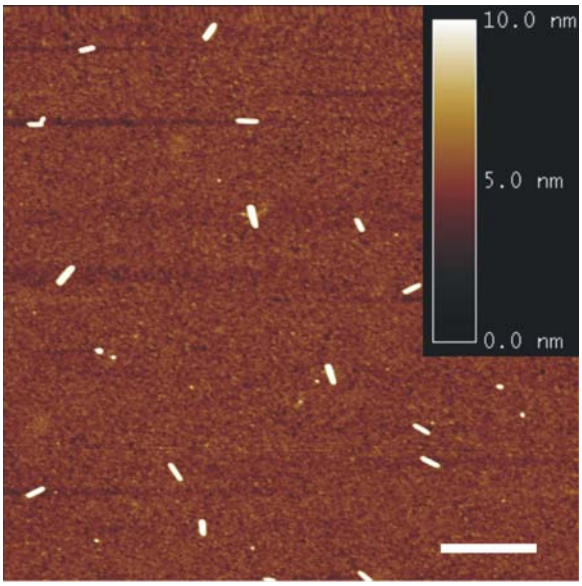

Figure 3.14: AFM image of iron (III) nanoparticles. The scale bar is 500 nm. See text for details.

3.4.3.2 Effect of applied potential

With a fixed charge of 5.0×10^{-4} C transferred, five different potentials (-1.0 V, -1.2 V, -1.4 V, and -1.6 V) were applied in a 10mM $FeCl_2 \cdot 4H_2O$ and 0.1 M H_3BO_3 solution. As seen on AFM images (Figure 3.15), the minimal applied potential required to obtain Fe (II) deposition is -1.2V. As the applied potential increases, nanoparticles started to clustering, and the clustering effect was extremely prominent at -1.6 V. The cubic particles are deposited optimally at the voltage of -1.4V

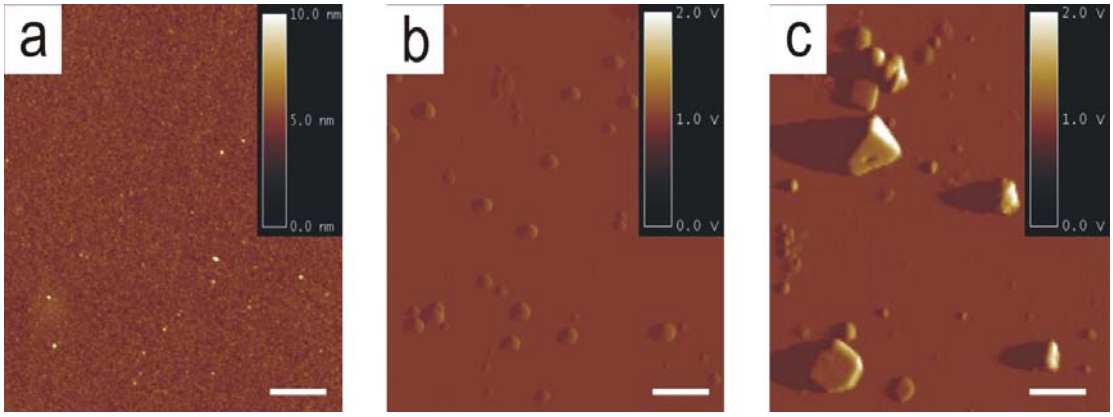

Figure 3.15: AFM image of iron (II) nanoparticles at different potentials: (a) – 1.0 V, (b) – 1.2 V, and (c) – 1.4 V. The scale bars are 500 nm.

3.4.3.3 Effect of applied charge

Particles of different shapes were obtained by varying the charge. With the increase of the charge, particles with more defined cubic structure were deposited. However, particles started clustering or forming film when the charge was too much. The optimal charge was found to be 5.0×10^{-4} C.

3.4.3.4 Effect of pH

The solution with different pH values were calibrated with 1M NaOH solution. With the increase of pH value, Fe (II) precipitates (probably as $Fe(OH)_2$), which decreased the amount of ferrous ions in the solution. At pH = 9, there was almost no deposited particle observed. At pH = 6, only rock-like particles were deposited. The optimal pH value to obtain regular sphere-shaped nanoparticles was at 4.

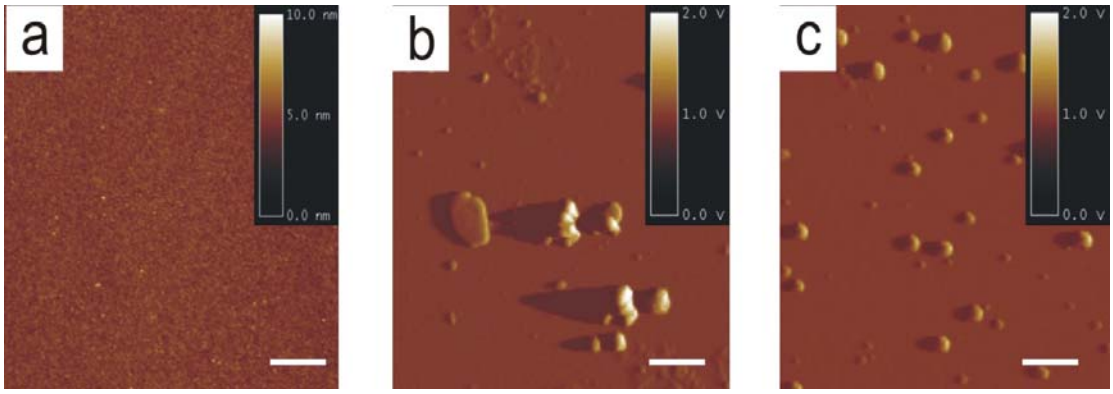

Figure 3.16: AFM image of iron (II) nanoparticles at different pH: (a) pH = 9, (b) pH = 6, and (c) pH = 9. The scale bars are 500 nm.

3.4.3.5 Uneven deposition

The deposition near the solution surface was much denser than inside the solution (cf. Figure 3.17). This might due to the interaction between the ions and the hydrogen from water. Near the solution surface, there were relatively less water molecules around each Fe^{2+} ion, and therefore the Fe^{2+} ions were more likely to deposit and grow bigger. However, more Fe^{2+} ions were involved in the hydrophilic interaction deep inside the solution. Another possible reason is that the electrons passed through from the top to the bottom of the Si wafer. As shown is Figure 3.13, the electrons passed solution – wafer interface first, so more electrons accumulated near the solution surface. However, the bottom wafer was inserted in the solution and less electrons left and reacted with Fe^{2+} ion.

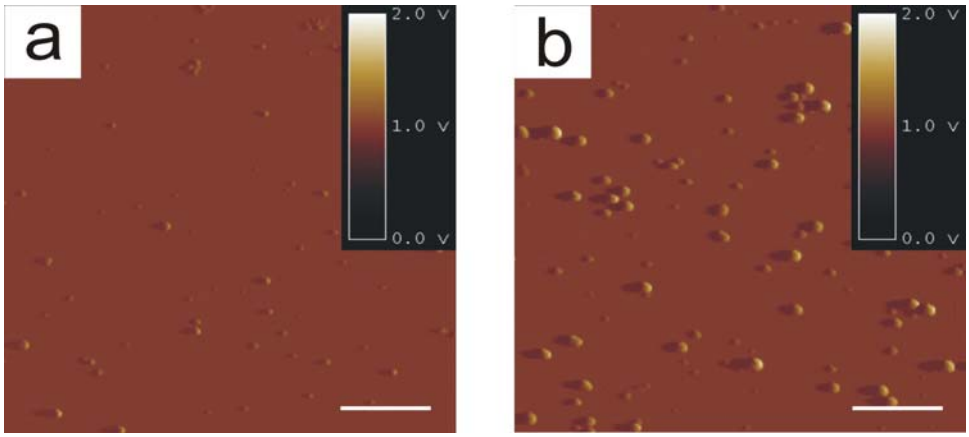

Figure 3.17: AFM image of iron (II) nanoparticles (a) near the surface, and (b) in the middle of the solution. The scale bars are 1 μm.

3.4.3.6 Deposition time

The size of the nanoparticles could be controlled by applying different deposition time with other parameters kept at the optimal condition. Larger nanoparticles were deposited with longer time, although the deposition within shorter time improved the uniformity of the nanoparticle size. Figure 3.18 showed controllable synthesis of iron particles.

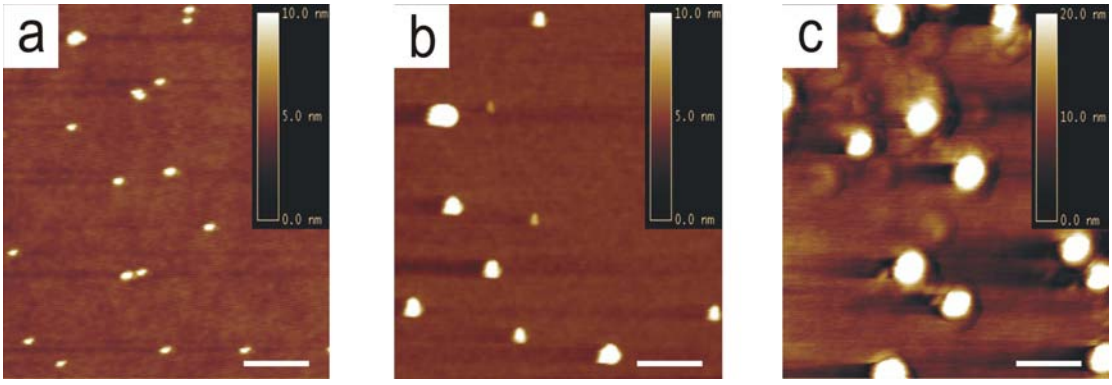

Figure 3.18: AFM images of monodisperse nanoparticles with diameters of (a) 7.2 nm, (b) 12.1 nm, and (c) 18.5 nm. The scale bars are 100 nm.

Figure 3.19: SEM images of monodisperse nanoparticles with diameters of (a) 7.2 nm, (b) 12.1 nm, and (c) 18.5 nm. The scale bars are 100 nm.

3.4.4 Conclusions and future directions

As shown in the figures, the iron particles with required sizes were produced as the prediction. Compared with wet chemical deposition, electrodeposition is more economical and harmless. Usually the wet chemical deposition requires 2-3 hours to generate iron particle, whereas electrodeposition only needs several seconds. Also electrodeposition does not contain organic solvent, which might bring tremendous harm to human heath or environment. With optimal experiment parameters, the control procedure could be simplified to adjust the time period.

Nanoparticles, particularly iron with its low-cost advantage, also have attracted peoples' attention due to their potential applications in spin-based electronics [62], data storage [63], and targeted drug delivery [64]. Nanoparticles with different shapes should have different electronic, optical, magnetic, and catalytic properties [65, 66]. Electrodeposition method could be one of the best candidates to generate nanoparticles with different morphologies.

The deposition of the nanoparticles is the first step to grow carbon nanotubes. A usable

nanotube requires sufficiently controlled physical parameters such as its diameter. We concluded that not only the size of the catalysts is very critical but also the interaction between catalyst particles and carbon atom. Although large catalytic particles are preconditions for growing large SWNTs, efficiency of carbon deposition on catalyst particle is also important for diameter-controlled SWNT growth. Therefore, we still expect the nanotube diameter is controllable under the optimized conditions based on various sizes of catalyst particles, such as temperature, gas flow rate, carbon source combination and growth time. The study of the growth of carbon nanotubes from these iron particles is still undergoing in our lab.

Chapter 4 Manipulation of Carbon Nanotubes

Nanomanipulation is a fundamental technique that is used in nanofabrication and to explore the interactions of entities at nanoscale. Carbon nanotubes have some unique mechanical and electrical properties, which makes them the ideal material for nanomanipulation. In this chapter, we will first present the details of sample fabrication techniques involved in this research. Then we will focus on two aspects: (a) the electrical breakdown of carbon nanotubes and (b) using AFM tips to manipulate SWNTs between two Pt electrodes. These projects will ultimately lead to the controllable assembling of nanotube electronic devices and better understanding of the interactions and mechanical properties of carbon nanotubes. Importantly, the synthesis of large diameter SWNTs is still ongoing in our research lab. As an alternative, namomanipulation technique offers a possibility to fabricate large cavity by extracting inner walls from a MWNT for our purpose. To obtain this amazing structure, we need to be able to cooperate and optimize the two technique mentioned in this chapter

4.1 Fabrication techniques of CNT devices

The fabrication process of sample CNT devices consists of, in sequence, the wafer preparation, patterning, and pattern transfer. As shown in the fabrication flow chart (cf. Figure 4.1), these process may be repeated if multi-layer processing is required. The patterning techniques using for patterns transferring is the photolithography in our experiments. Depending on applications, pattern transfer can be accomplished through thin

film deposition or etching. In our lab, at first step, the design and arrangement of the devices were accomplished by Adobe Autocad. Our design was shown on Figure 4.2.

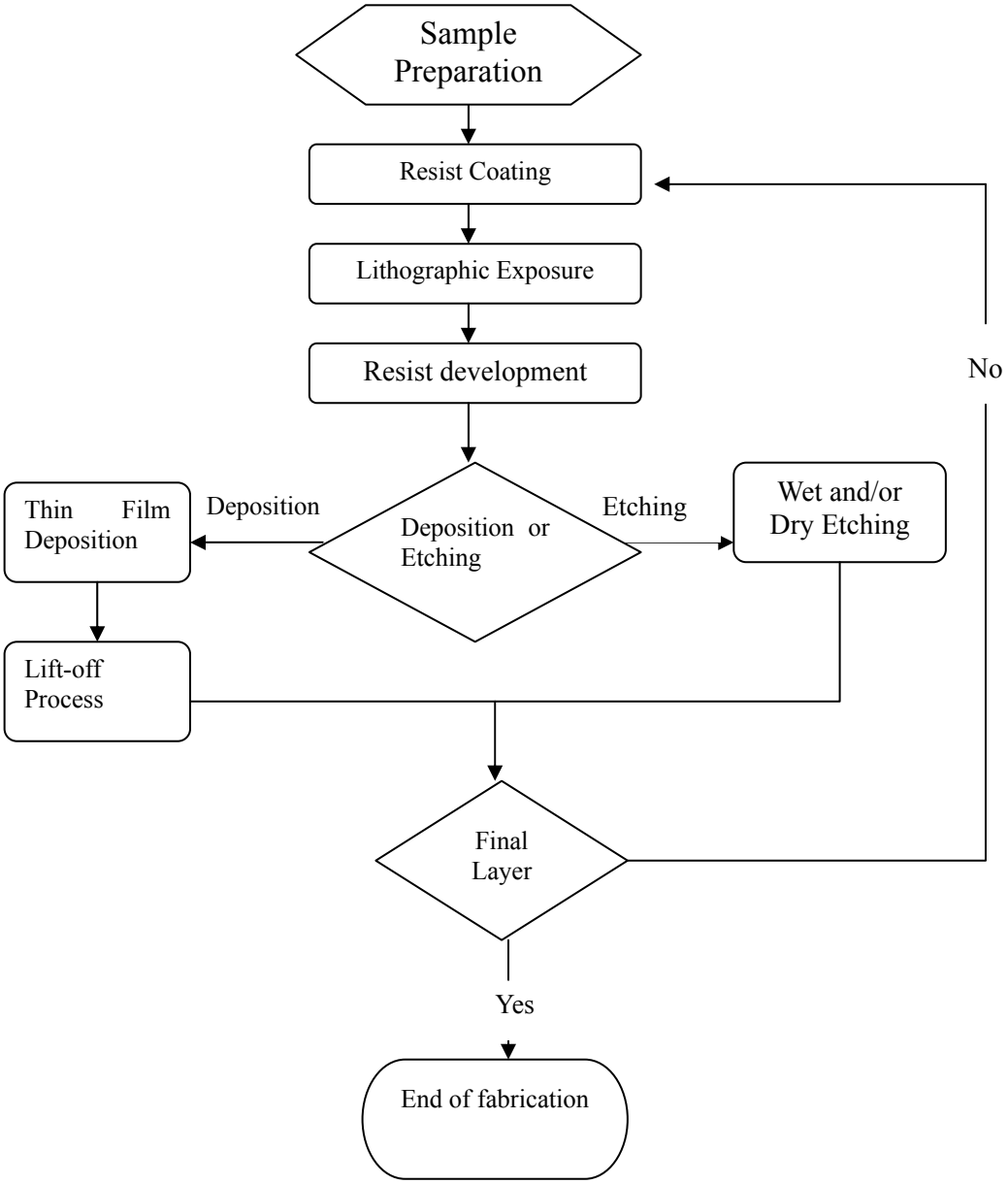

Figure: 4.1: Process flow of typical patterned CNT device fabrication

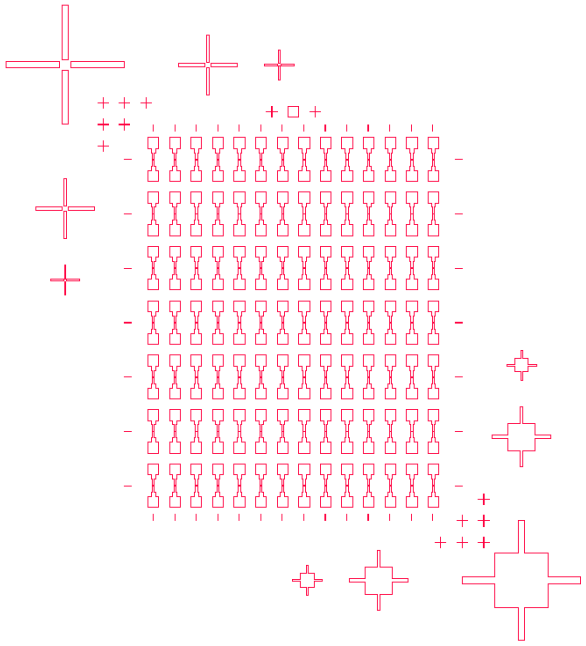

Figure 4.2: The design of patterned CNT device using Autocad software

4.1.1 Wafer preparation

Commercial silicon wafers were used in our lab. In the early experiments, non-doped wafers were polished on one side with 300 nm thermal oxide layer for insulation. The substrates were essentially insulated at low temperatures. For backside gated experiments, commercial highly doped silicon wafers were utilized which were polished on one side with 500 nm thermal oxide layer. In those wafers, the silicon stayed conductive even at low temperatures and was used as a backside gate.

Since the surface properties would influence the transport measurements, the wafers were carefully cleaned in several steps: cleaned with acetone in the ultrasonic bath for 15 minutes, followed by the same steps with methanol and isopropyl alcohol, and finally dried by N_2 gas. The cleaning process should clean off any dust generated by dicing, and remove

any organic and inorganic contaminations. At the end of the process, the isopropanol should come off the wafer surface uniformly without forming droplets. Otherwise, the wafer was not clean enough and the cleaning process should be repeated.

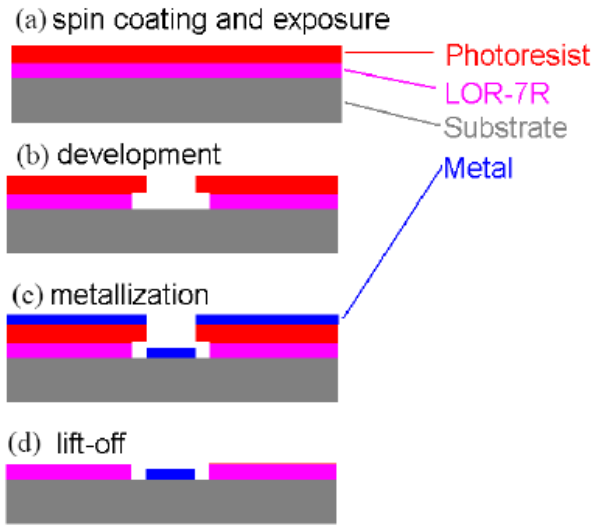

Figure 4.3: General Steps in the photolithographic process. (a) Spin coat two layers of resist and expose, (b) the development opens windows on the substrate, and the bottom layer is more sensitive to exposure, which results in an undercut, (c) coating metal, and (d) lift-off the resist, leaving only the metal on the substrate.

4.1.2 Photolithography

Ultraviolet (UV) photolithography was used as the key technique for making the mask of desired shape and size with a resolution down to 100 nm. By using this photolithography, the mask of big pads (>500 nm), markers as well as the electrodes of desired shape were made. A schematic explanation is presented in Figure 4.3 and the procedure details are listed below:

1) Spin lift-off resist LOR 7B4 at 3000 rpm for 60 seconds for a 750 nm thick coating.
2) Bake the substrate in a convection oven at 170 °C for 30 minutes.
3) Spin Shipley 1813 photoresist at 3500 rpm for 60 seconds for a 1.5 μm thick coating.

4) Bake the substrate in a convection oven at 110 °C for 30 minutes.
5) Put the substrate in a Karl Suss Mask Aligner and expose the substrate under a 350 W spotlight halogen lamp for 30 seconds.
6) Mount the substrate on spinner and spin at 500 rpm. Develop the pattern by spraying developer on the substrate for 1 minute, followed by spraying DI water for 1 minute. The substrate is then spun dry at 5000 rpm for 1 minute and blew dry.

4.1.3. Plasma etch

For most of the samples, a plasma etch was used for various reasons. Photolithography cannot completely remove photoresist and leave a very thin layer of the residue. The residue poses a problem for metallization and lift-off. A short-time O_2 plasma etch was needed for removing the photoresist residue while minimizing the unwanted etches on the unexposed photoresist.

4.1.4 Thin film metal deposition

In our experiment, 50 nm of platinum (Pt) on top as electrode layer and 2 nm of titanium (Ti) as a stick layer beneath were deposited by Electron Beam Physical Vapor Deposition (EBPVD) in University of Macmaster.

4.1.5 Lift-off process

The sample is fully covered by the thin film after metallization. Lift-off process was used to remove unwanted parts of the film. Different lift-off processes were used depending on what kind of resist was used for patterning. The sample was immersed in acetone and a

syringe was used to shoot acetone on the sample surface to facilitate lift-off. If the unwanted metal does not come off immediately, the sample will be soaked in acetone for some time. Process time of lift-off can vary from 15 minutes up to overnight depending on the condition of the photoresist. The sample is rinsed by clean acetone, and then rinsed by isopropyl alcohol before being blown dry by N2 gas. After lift-off, the devices with catalyst islands were fabricated as Figure 4.4.

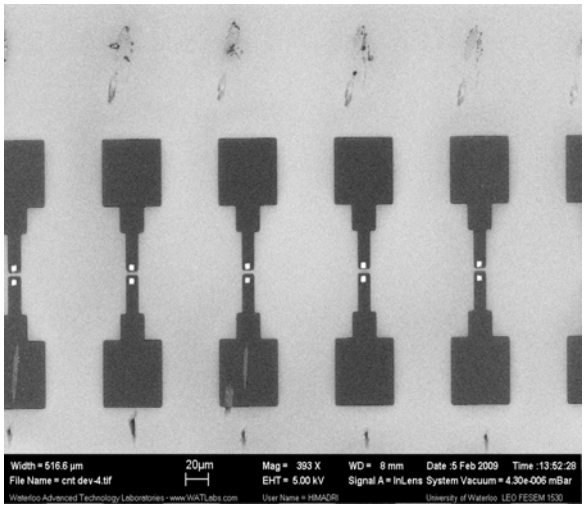

Figure 4.4: SEM image of the devices after lift-off litoffliftohyhvilffabrication process, where the metal coating is Pt.

4.1.6 Carbon nanotube growth on devices

After the steps above, we obtained the device in Figure 4.4, which was ready for further fabrication. In this research, single-walled carbon nanotubes were grown by CVD method, which is summarized as below:

1) Silica supported catalyst preparation: mix 6 mg of iron acetate, 10 mg of cobalt acetate, 1.5 mg of molybdenum (II) acetate, 25 mg silica (aerosol 380 D11092D) in 10ml of deionized water and sonicate for 2 hours.

2) Substrate preparation: Cut out a single chip (with an array of 14×7 devices) by diamond scriber and check under microscope to inspect the photoresist pattern.

3) Catalyst deposition: spread the catalyst on the cleaned wafer by spin coating and lift-off by acetone.

4) CVD synthesis: place the wafer into the CVD chamber with all gas lines open. Methane and ethylene was inserted as carbon source under 850°C for 10 min. Hydrogen was also accompanied as carrier gas.

After completing those steps, SWNT device was achieved as shown in different angles of view. (Figure 4.5-4.7)

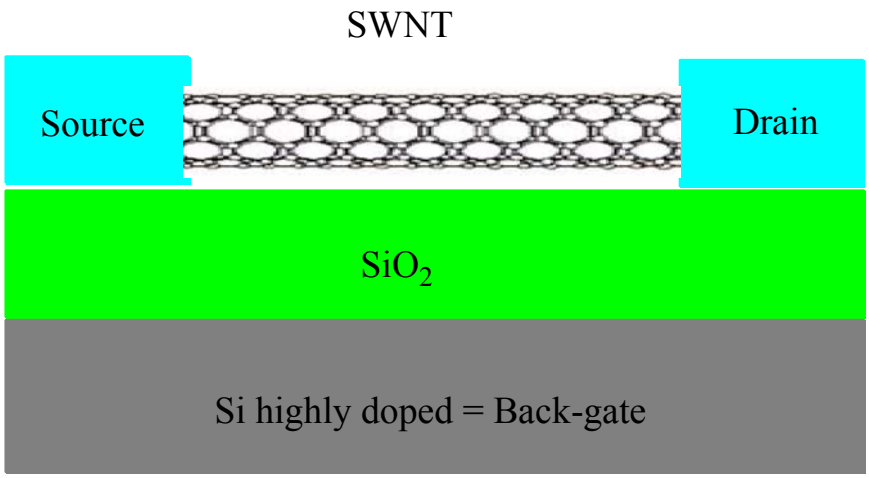

Figure 4.5: Schematic diagram of side-view SWNT device after fabrication

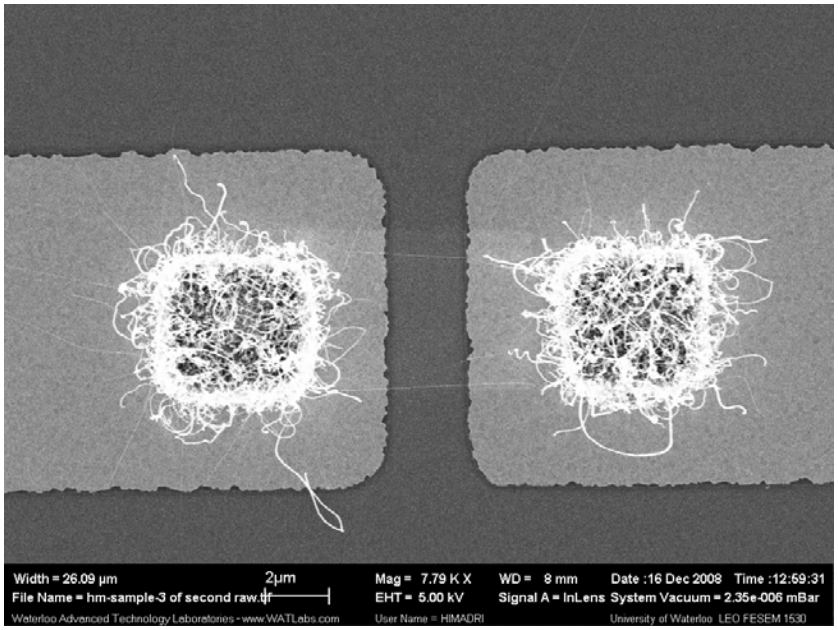

Figure 4.6: The SEM image of two catalyst islands on different electrodes bridged by SWNTs grown using the CVD method.

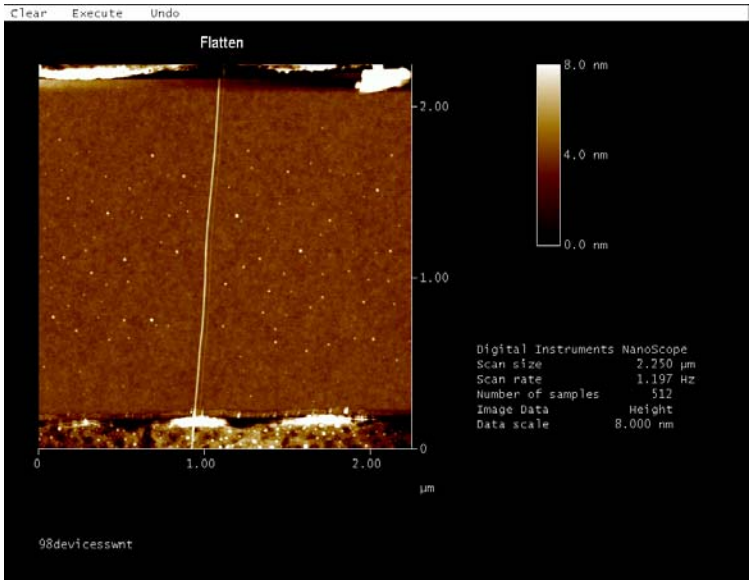

Figure 4.7: AFM image of two catalyst islands on different electrodes bridged by one SWNT grown using the CVD method.

4.2 Measurement Setup of CNT devices

The carbon nanotube devices are put under a microscope. A homemade probe station with sharp needles is used to make contact with the electrodes of the device. Once electrical contacts are achieved, electrical properties of carbon nanotubes can then be tested. The nanotube device has two electrodes at the two ends of the device and a third electrode, called the gate, the silicon substrate underneath the nanotube, which is electrically insulated from the nanotube by an insulator (typically silicon dioxide). However, by applying a voltage across the nanotube and the gate, a capacitor can be formed and charged. By varying the voltage, the amount of charge on the nanotube can be changed.

The current between the two contacts on the nanotube is monitored while varying the gate voltage (changing the amount of charge on the nanotube) (cf. Figure 4.8). Based on the measurement of monitored current changes, carbon nanotubes can be categorized into two types: (a) metallic nonotubes, when the current stays constant as the gate voltage changes (cf. Figure 4.8a), which is similar to metals, and (b) semiconducting nanotubes, in which the current drops dramatically as the gate voltage increases (cf. Figure 4.8b). The applied gate voltage allows adding charges to the nanotube, and makes it conductive. Applying negative gate voltage will add "holes" (positive charges corresponding to the absence of an electron) to the nanotube, which makes the conductibility better. At around zero gate voltage, there are no holes, and the nanotube stops conducting. (We should note that the nanotube should conduct again at a positive enough voltage which would add negatively charged electrons to the nanotube, but it does not because of the barrier at the metal-nanotube interface.)

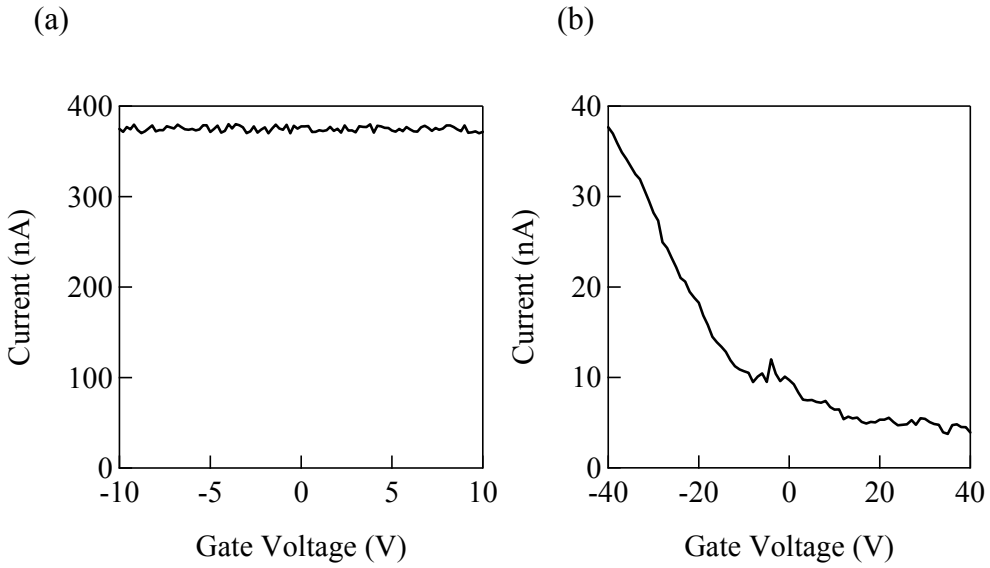

Figure 4.8: Current as a function of gate voltage for (a) a metallic nanotube, and (b) a semiconducting nanotube.

4.3 Electrical Breakdown of Carbon Nanotubes

4.3.1 Electrical breakdown of SWNT devices

4.3.1.1 Brief introduction

SWNTs have attracted great interest for some years due to their unique exciting electronic properties and potential use for nanoelectronic applications, e.g. interconnects or transistors. [67] To evaluate their properties and potential applications, it is necessary and important to gain much more detailed understandings of their behaviors in terms of biases and electrical breakdown. In the synthesis, SWNTs always have different electronic properties, which make it difficult to directly integrate SWNTs into electronic devices. For the two types of SWNTs, semiconducting nanotubes with a high on/off current ratio are required for transistors while metallic nanotubes are for interconnect. Furthermore, there are

two different metallic SWNTs with different behaviors, i.e. armchair SWNTs, which have truly metallic characters and quasi-metallic SWNTs, which have a small curvature-induced band gap. Methods to separate semiconducting and metallic nantubes have been proposed. However, due to the lack of precision, poor yield and necessity of electronic characterization of separated material, these methods need be further improved. [68]

Among the existing methods, preferential breakdown is a straightforward method to eliminate nanotubes. In semiconducting SWNTs, an appropriate positive gate voltage is applied to deplete the nanotubes before increasing the bias. Due to the current carrying capability of individual metallic SWNTs, self-heating by electrophonon scattering processes and thermal oxidation can deplete the metallic SWNTs. Electrical breakdown of individual SWNTs has applied to determine the proportion of semiconducting SWNTs. [69]

The preferential electrical breakdown of the nanotubes determines the performance of high-current nanotubes transistors to a large extent. [70] These transistors were built by parallelly arranging a large number of SWNTs which grow randomly. To optimize the performance of high-current nanotube transistors, it is necessary to understand the electronic breakdown of SWNTs with various electronic properties. The study about the temperature transport characteristics of a SWNT with small diameters is conducted under the room temperature.

4.3.1.2 Experimental setup

The geometry of the device in this thesis is shown in Figure 4.9. On top of an insulating material layer, a SWNT connected two metallic contacts. The top of the nanotube was not covered and exposed to ambient. The range of SWNT diameters range was $0.8 < d < 2.2$ nm

obtained from AFM cross-section measurements. The silicon wafer beneath was used as a back-gate for turning on the tubes.

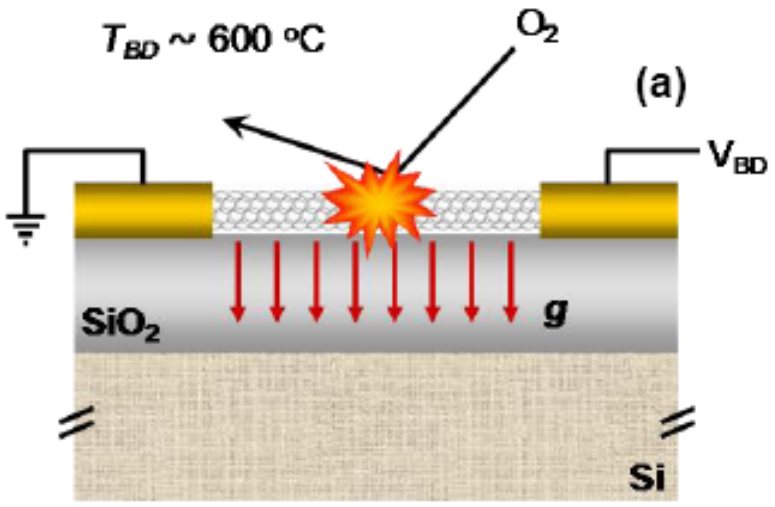

Figure 4.9: Schematic of oxidation-induced SWNT breakdown, when exposed to air at high applied voltage. The length of the nanotube portion between the contacts is L; the heat conductance into the substrate per unit length is g (red arrows). [71]

4.3.1.3 Experimental Results and Discussions

4.3.1.3.1 Electrical breakdown of a single SWNT device

Optically, a SWNT during electrical breakdown event was captured by AFM in Figure 4.10. Electrically, when the voltage was increased, a 17μA current drop was observed at 18 V as shown in I-V curve. After the current drop, bias sweeps showed current carrying capacity was almost 0, which indicates the SWNT was permanently damaged. (Figure 4.11)

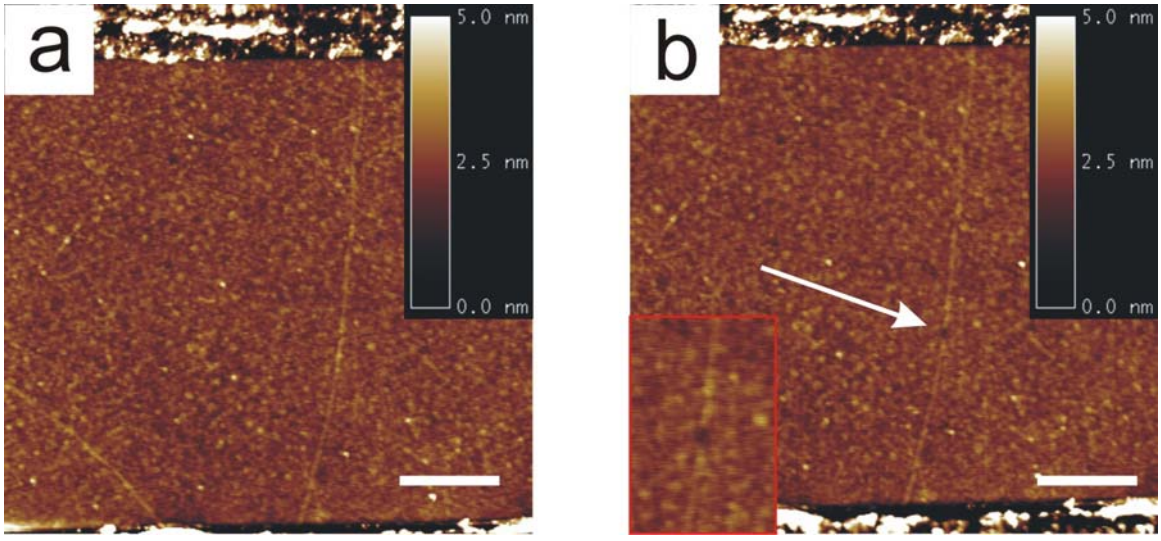

Figure 4.10: AFM images of before (a) and after (b) electrical breakdown of single SWNT device. Scale bars are 500 nm.

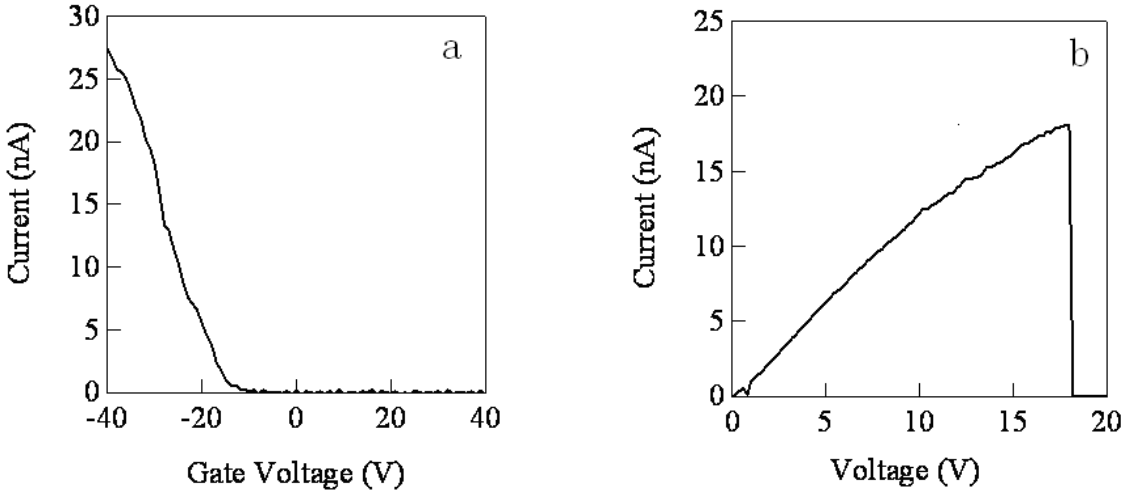

Figure 4.11: Electrical breakdown of a single SWNT device
(a) Ids-Vg curve of a semiconductor SWNT device before electrical breakdown
(b) I-V curve of electrical breakdown of a SWNT device (Vg=-40V)

According to the theory proposed in [72], the linear expression of breakdown power for the nanotube with the length > 1μm (Figure 4.9) can be calculated as following:

$$P_{BD} \approx g\,(T_{BD}-T_0)\,L \qquad (3)$$

The breakdown voltage is $V_{BD} = P_{BD}/I_{BD}$, where T_{BD} is the breakdown power and P_{BD} is the minimum power that makes the nanotube reaches the breakdown temperature T_{BD}. The formula does not include thermal conductivity k, which indicates the Joule heat is not dissipated into contacts, but down into the substrate (Figure 4.9). T_0 indicates original temperature before voltage is applied and L is the length of the nanotube portion between the electrode contacts. A range for the heat sinking coefficient $g \approx 0.15 \pm 0.03$ $WK^{-1}m^{-1}$ (g: the heat conductance into the substrate per unit length) found in Ref. [6]. In our experiment, the average length L is about 2.8 μm, $P_{BD} = V_{BD}I_{BD}$= 17μA x 18 V = 306μW, T_0 = 300K. Using the above formula, we can predict the breakdown temperature.

$$306\ \mu W = 0.18 WK^{-1}m^{-1}(T_{BD} - 300K) \times 2.8\ \mu m$$

$$T_{BD} = 907K$$

As calculated, the breakdown temperature (634ºC) was consistent with the known breakdown temperature of SWNTs from thermogravimetric(TGA) analysis of bulk sample.[73,74]

4.3.1.3.2 Electrical breakdown of a multiple SWNTs device

We also studied the breakdown behavior of a multiple SWNTs device. AFM images (Figure 4.12 and 4.13) showed both before and after electrical breakdown images. In these two images, two SWNT breakdowns happened in the same device. Also, Figure 4.14 illustrated the I-V curve before and after the breakdown of a two SWNTs device. At high bias around 7 V, two current dropped which were 17 μA and 20 μA were observed in sequence.

The average current drop of 19μA was close to the theoretical prediction of 23 μA current drop in SWNTs. [75]

After complete breakdown, we noticed that the electrical breakdown sites almost concentrated in the middle of SWNTs. As mentioned in previous literature [76], in a SWNT, the heat radiates in a diffusive mode rather than a ballistic mode. Therefore, the possible cause is that the middle of a SWNT is far from the electrodes which make it difficult to diffuse the heat. On the other hand, the segments of a SWNT in contact with the metal electrodes are much easier to radiate the heat, and that is why the centre of a SWNT has the highest temperature which leads to the breakage of the nanotubes.

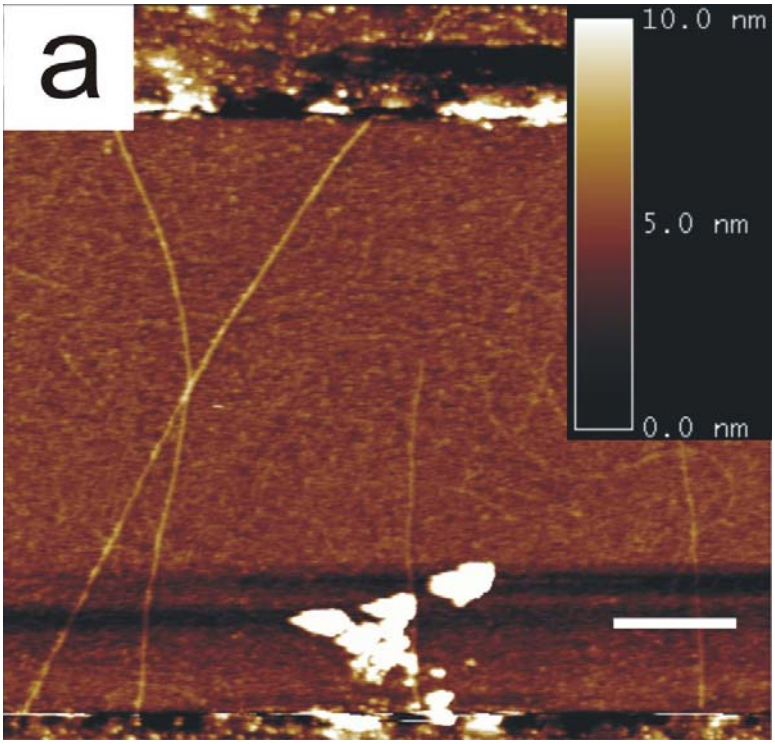

Figure 4.12: AFM image of a multiple SWNTs device before electrical breakdown

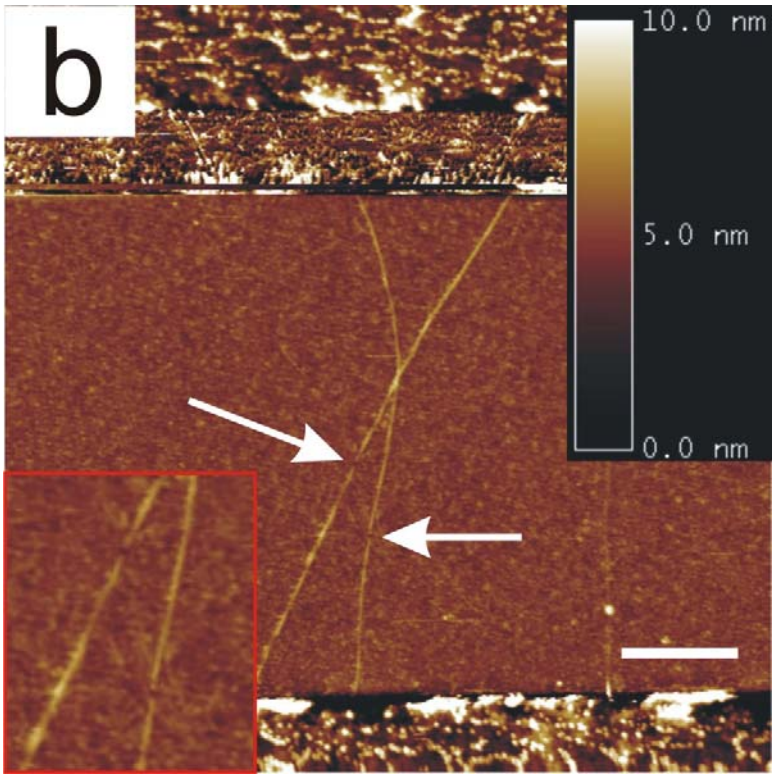

Figure 4.13: AFM image of a multiple SWNTs device after electrical breakdown Scale bar is 500 nm

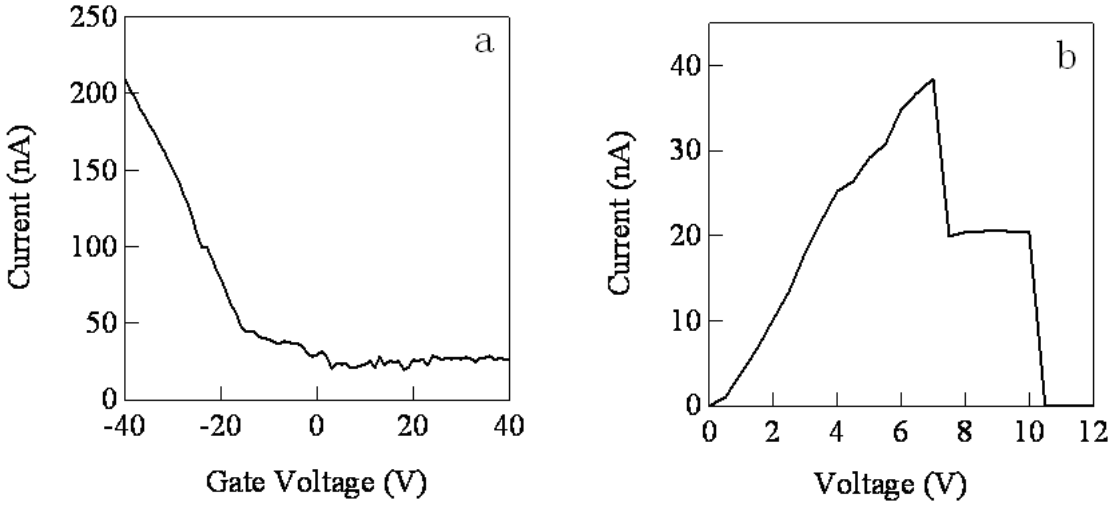

Figure 4.14: Electrical breakdown of a multiple SWNTs device
(b) Ids-Vg curve of a multiple semiconductor SWNTs device before electrical breakdown
(b) I-V curve of electrical breakdown of a multiple SWNTs device (Vg=-40V)

We presented the results on high-bias transport in both single SWNT device and multiple SWNTs device with a focus on the mechanism of current saturation and field-induced electrical breakdown. Also, electrical breakdown of SWNTs offers a powerful tool to separate semiconductive SWNTs and metallic SWNTs.

4.3.2 Electrical breakdown of MWNT devices

4.3.2.1 Introduction

MWNTs are promising and reliable materials for nanometer-sized wires and microcircuit interconnects since their large diameter enables efficient conduction at high biases. Moreover, the unique structure of concentric shells provides a superior mechanical rigidity. The recent studies on transport property of MWNT use a “side contact” technique, [78] the MWNT are deposited on two Pt electrodes, which are pre-patterned to make the outermost wall contact with the electrode but the inner walls be free from the electrode. Consequently, parallel conduction along the inner walls has litter interference to the overall current, which is proved by experiments that shows current only flows in the outermost wall in side-contacted MWNTs [79]. Characterization of the conductivity of side-contacted MWNTs has been investigated by using an electric breakdown technique but it is complicated due to the fact that tunneling barrier is derived from the side contact geometry [80]. A novel method has been used to study transport properties of MWNTs, in which an “end contact” is used to make every single wall of MWNTs contact with electrodes [78]. This contact configuration allows the study of transport in multiple-layer systems, which makes the study of transport properties of each wall within a MWNT feasible. In the above section,

the electrical breakdown of SWNTs has been well exhibited and discussed. Many electronic devices based on these properties have been designed [77]. However, in the case of MWNTs, the transport properties have not been fully understood because of their extremely complex structures which nest many SWNTs with different electronic structures. The electrical breakdown of MWNTs is crucial for their applications because it determines the maximum current through a nanotube.

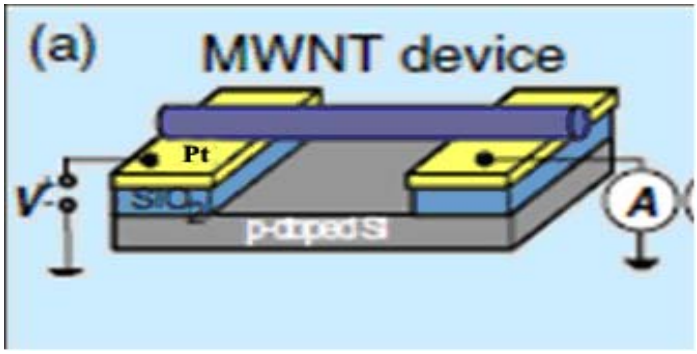

Figure 4.15: An illustration of a typical MWNT device with source, drain and back gate. The SiO_2 is insulating, making it possible to use the Si as a back gate.

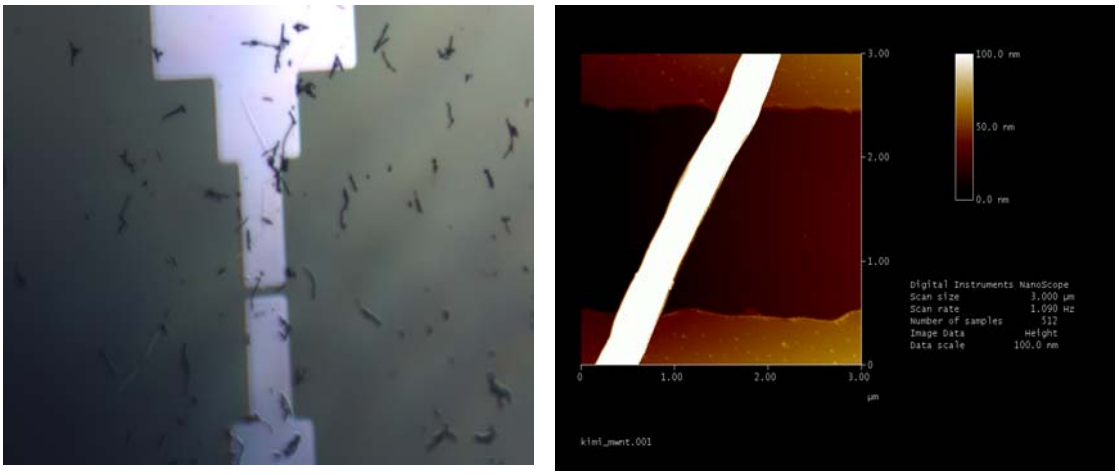

Figure 4.16: Images of a MWNT deposited on two Pt electrodes to fabricate devices (a) Optical image (b) AFM image

4.3.2.2 Experiment details

MWNTs purchased from Sigma-Aldrich were dispersed in a combination of 80% dichlorobenzene and 20% isopropanol. And then they were purified to remove amorphous carbon and some aggregates by centrifuge. These purified MWNTs were spin-coated on Pt electrodes and baked overnight. After these procedures, MWNTs devices were fabricated as shown in different ways. (Figure4.15 and 4.16) Finally, the electrical breakdown of MWNT experiments were performed by applying a constant voltage to a MWNT device while acquiring the current drop across each carbon shell failed and physical cut in a AFM image.

4.3.2.3 Results and discussions

We performed the electric breakdown to investigate the electronic properties of MWNT devices. Figure 4.17 showed the time-resolved electrical breakdown of a 187.34 nm MWNT in air. The constant voltage was applied at 1.6 V, so the current was a function of time I (t). The series of 8 abrupt current drops were observed with similar step sizes of 18 μA except the second step and the fifth step. In the second and fifth step, 35μA and 34μA drops might due to the electrical breakdown of two layers at the same time.

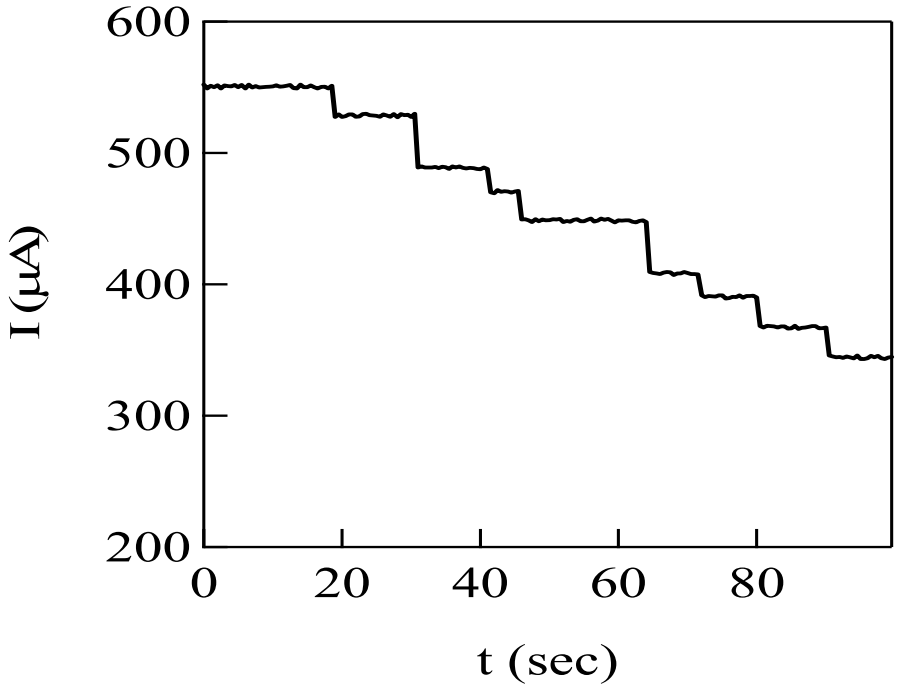

Figure 4.17: The partial electrical breakdown of a MWNT at constant voltage (1.6V)

Except for investigating MWNT breakdown electrically, we used AFM to image MWNTs before and after electrical breakdown. Images of thinned MWNTs showed large quantities of lost carbon (Figure 4.18 and 4.19). Figure 4.17 showed the total number of discrete steps N observed in the breakdown, which was considered as a function of the initial diameter of the MWNT determined by AFM. Dependence between N and the MWNT diameter was identified in this figure. To first approximation, it was proportional to the number of shells in the MWNT. Based on AFM cross-section measurement (see Figure 4.19), diameters of 187.34 nm and 184.02 nm were obtained before and after the breakdown

respectively. According to:

A decrease in diameter = the intershell spacing (0.34 nm) X the number of completed breakdown steps N [15]

3.32 nm decrease in diameter is approximate to 10 layers breakdown which is consistent with the observation on the Figure 4.17

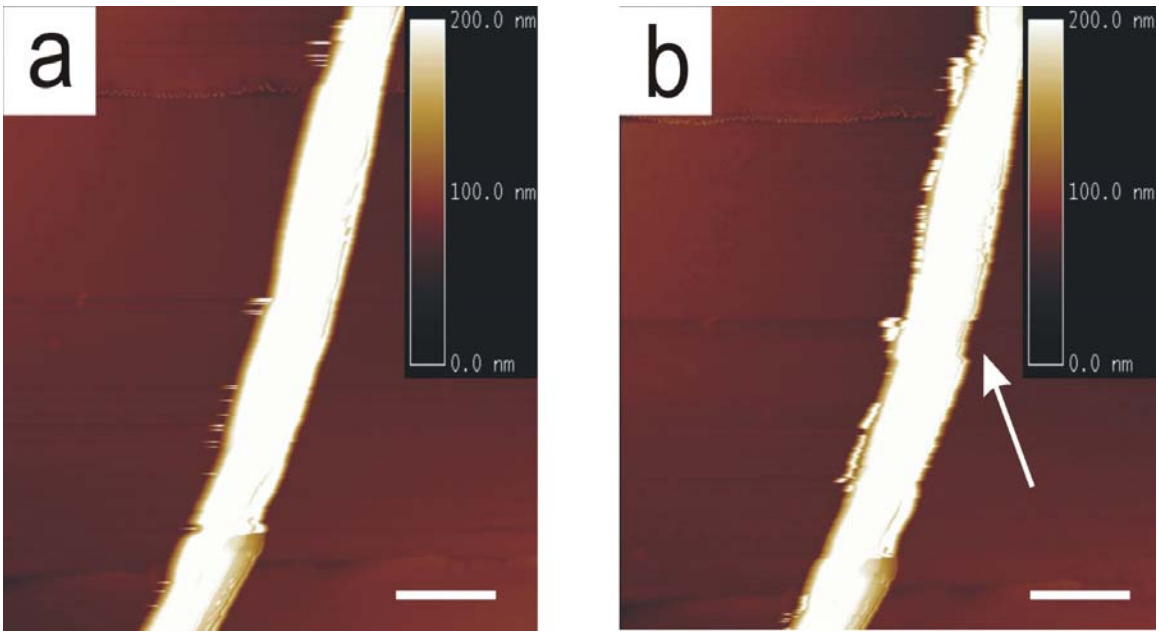

Figure 4.18: AFM images of before (a) and after (b) electrical breakdown of a MWNT device

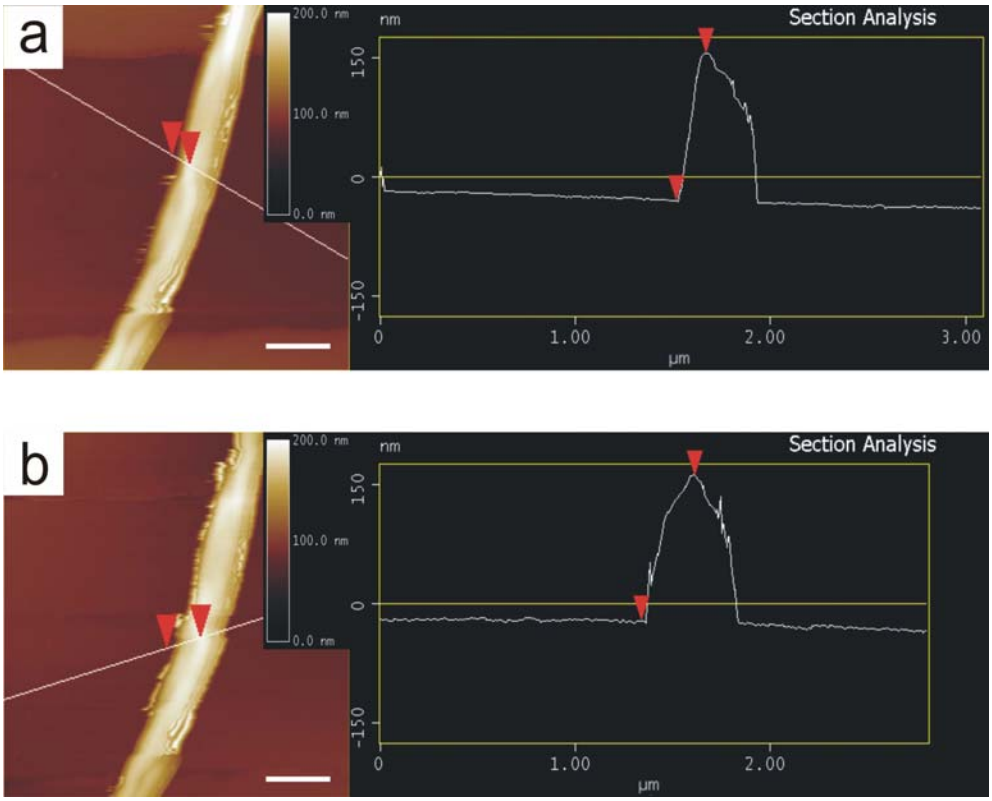

Figure 4.19: AFM cross-section analysis of electrical breakdown of a MWNT device (a) 187.32 in diameter before (b) 184.02 nm in diameter after.

Our observations indicated that several shells may contribute to the high bias conductance of a MWNT, whereas Bachtold [82] believed the single-shell model holds in the low bias and low temperature regime. As shown in the experimental result, the breakdown voltage of SWNT was much greater than MWNT. It means that the multi-shell structure improves the conductance, which enables the large current on the outermost shell with the low voltage. This difference is probably due to the energy dependence of intershell coupling. At high biases, two factors may make the effective coupling improved. One is the electron

injection at the contacts. The other is the enhanced electron-electron scattering, which will tend to relax momentum conservation requirements among shells.

Electrical breakdown prefers to happen on the outermost layer which is in direct contact with the metal electrodes. A possible explanation is that outer shells contribute more than inner shells to the total conductance in this geometry because of their lower coupling resistance to the external electrodes. Also the presence of oxygen surrounding the outer layer facilitates the breakdown process.

For the further understanding of current saturation and uniform current steps during breakdown, obviously there is a great demand of the improved models of MWNT conduction.

During the experiments, we observed two type of breakdown: “Step Breakdown” and “Cliff Breakdown”. (Figure 4.20 and 4.21)

The experimental results of “Step Breakdown” show that the breakdown happened when passing a current of 68 μA. The current caused a five-walled nanotube segment which was eliminated wall-by-wall by electrical breakdown in the time sequence. Similar to Figure 4.17, the loss of one wall results in an instant current drop, as shown in Figure 4.20. The current dropped approximately 18μA, 30μA, 23μA, 25μA and 27μA respectively as the first five stepwise walls breakdown happened.

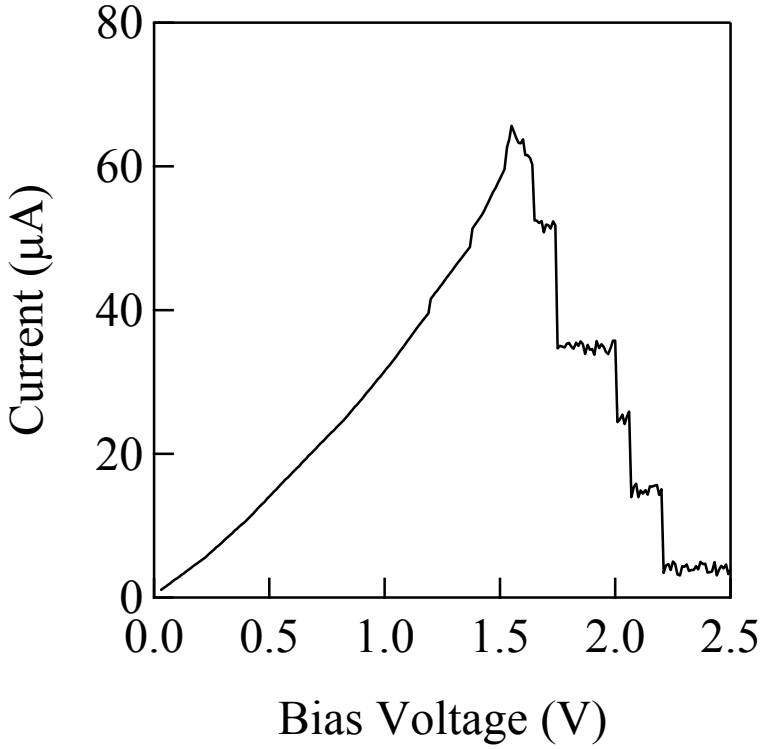

Figure 4.20: I-V curve of "Step Breakdown" of a MWNT device

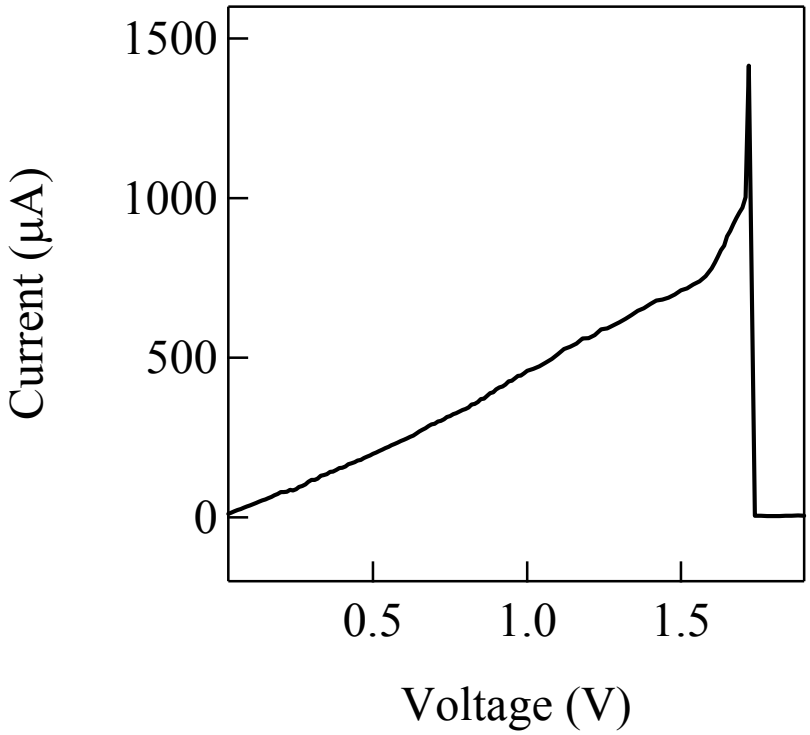

Figure 4.21: I-V curve of "Cliff Breakdown" of a MWNT device

The I-V curve in Figure 4.21 showed “Cliff Breakdown” happened at nearly the same bias voltage as that in “Step Breakdown”, even though the magnitude of their peak current I_{peak} varies dramatically. And MWNTs which were in between two Pt electrodes disappeared from AFM. In order to explain these phenomena, we notice a similar constant breakdown voltage has been reported on the current-induced break of metal nanocontacts.[83,84] Fujii [85] proposed a possible break mechanism of metal nanocontacts based on electromigration of metal atoms, although the details are still under investigation. Accordingly we assume that the experimental result in Figure 4.21 can be attributed to the movement Pt atoms of electrodes. Electrode atoms at the contact would be free to move in the high-bias regime, and their massive migration is likely involved in the contact modification when the irreversible current increases in the “Cliff Breakdown”. This may also explain why MWNT disappeared after electrical breakdown in AFM. But similar to the break mechanism of metal nanocotacts, it is still unknown that whether the electromigration is a primary breakdown mechanism of MWNTs and how it causes the constant break voltage.

In conclusion, two distinct high-bias breakdown behaviors were discovered during our experiment, which are designated as “Step Breakdown” and “Cliff Breakdown”. The “Step Breakdown” typically reveals the current drops in a stepwise manner, which suggests the shell-by-shell breakdown. We inferred that the “Step Breakdown” is caused by homogenous heat generation due to substantial electron-phonon scattering inside the nanotube. The “Cliff Breakdown” is characterized by the steep pre-breakdown increase in current along with the irreversible changes in the I-V characteristics. We believe that the “Cliff Breakdown” is contact-related and occurs at MWNT/Pt contacts. It is likely that the short effective length of our MWNTs would lead to the local heat dissipation near the contact and make it possible to

observe the contact-related breakdown.

4.3.2.4 Conclusions and future direcitions

Electrical breakdown provides an easy and reliable way to cut and open CNTs. The controllable electrical breakdown is a powerful technique to figure out the transport properties of complex CNTs. Also, our study reveals the possibility to create large cavity of MWNTs by extracting inner shells from MWNTs in the future direction. Moreover, comparing different kinds of MWNTs and measuring other their properties during the electrical breakdown should be vital for evaluating their possible applications in promising devices.

4.4 AFM manipulation on SWNTs

4.4.1 Introduction

Although AFM manipulation experiments have been reported on MWNTs, [86] it is harder to carry out the same experiment on SWNTs because the diameter is several orders of magnitude smaller. However AFM manipulation experiments were successfully achieved on individual SWNTs on silica surface recently, where the tip of an AFM was used to bend nanotubes. Also, tapping-mode AFM measured the height as a function of the feedback parameters, which showed that nanotubes appear lower in height in AFM image than expected. [86] This might result from a local and reversible compression of the nanotubes by the tapping tip. Also, manipulated buckles and crossings are slightly more rigid than individual non-manipulated nanotubes, as shown in the height measurements.[86]

For our purpose, to create large cavity of MWNTs, the primary step is to manipulate

nanotubes with AFM. In this section, we successfully created the carbon nanotube junctions by using the tip of AFM to change the shape of individual SWNTs and their positions of them on the surface of silica. This manipulation technique can be applied to bend nanotubes.

4.4.2 Experimental method

In tapping-mode AFM, the range of oscillation amplitude is 1 to 10 nm which was achieved by a stiff cantilever, with which a sharp tip was attached and oscillated near resonant frequency. The amplitude of oscillation was decreased when the tip contacted the sample surface and also kept changing when the height of the sample surface changed. To maintain a constant setpoint amplitude, a feedback loop was used to change the height of the cantilever over the surface. And because the contact of tip with the sample was only intermittent, the lateral forces imposed on the sample during scanning are negligible and thus the individual SWNT grown between two Pt electrodes on Si wafer was imaged exactly without movements. However, if the feedback was off, the cantilever was pressed down into the substrate and dragged along a predefined path, and then the nanotube was shifted laterally. Based on this, the manipulation of SWNTs was accomplished. In the manipulation experiments, AFM diamond tips which were stiffer than normal silicon tips were mounted with stiff cantilevers having a constant force and a resonant frequency of around 200 kHz.

4.2.3 Result and discussion

A typical manipulation experiment of a carbon nanotube was demonstrated in Figure 4.22. As can be seen, the tube was dragged from its original position and was bent strongly and held by Van Der Waals binding to the substrate. In tapping mode, the tip was scanned

over the sample to identify a nanotube and then was pressed onto the surface and moved along a predefined path. As a result, the position and shape of nanotubes could be controlled accurately. The initial configuration of a straight nanotube was grown across two electrodes and then the nanotube was dragged across the surface in a direction perpendicular to the length and thus the tube was bent between the middle two electrodes, with a bent angle of 30º.

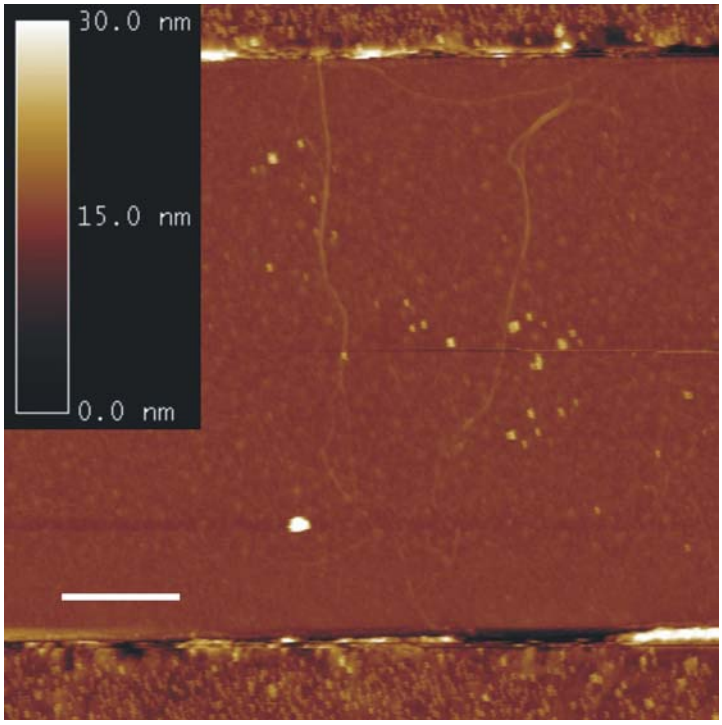

Figure 4.22: AFM image of "kink" formation of a SWNT

4.2.4 Conclusions and future directions

The manipulation of individual SWNTs which can create artificial nanotube junctions is similar to that of molecules with an STM. [87] The manipulation of nanotubes into buckles and bends makes transport studies of junctions in nanotubes possible. The transport studies of nanotube ropes [88] and nonotube kink junctions [89] demonstrate interesting properties of molecular junctions. The transport studies of manipulated junctions show that a two-terminal

room-temperature resistance of nanotube buckles is about 1 ~ 10 MΩ, much higher than that of non-manipulated nanotubes.[90]

Manipulation of the shape, position and alignment of nanotubes can be controlled as that the nanotube segments are pushed in a predefined way. Because AFM tip is a very useful tool to manipulate individual nanotubes in a controlled way, it is feasible to further study the performance of the manipulation technique by fabricating a more complex pattern and therefore makes it possible to study the electrical properties of nanotubes as a function of shapes and alignments.

In the future work, more characterization experiments to monitor the changes of SWNT properties after manipulation need to be carried out in our lab. Furthermore, extracting inner shells out of a MWNT to make large cavity carbon nanotube becomes possible by this AFM tip manipulation technique. As we mentioned before, the “brand new” structure of carbon nanotube will be applied for many promising applications in various areas.

References

[1] Iijima, S., *Helical Microtubules of Graphitic Carbon.* Nature, 1991. **354**: p. 56.

[2] Iijima, S., Ichihashi,T, *Single-shell carbon nanotubes of 1-nm diameter.* Nature, 1993. **363**: p. 603.

[3] Bethune, D.S., Kiang, C. H., Devries, M. S., Gorman, G., R. Savoy, R., J. Vazquez, J., and Beyers, R., *Cobaltcatalyzed growth of carbon nanotubes with single atomic layer walls.* Nature, 1993. **363**: p. 605.

[4] Radushkevich, L.V., Lukyanovich, V. M., *O strukture ugleroda, obrazujucegosja pri termiceskom azlozenii okisi ugleroda na zeleznom kontakte.* Zurn Fisic Chim, 1952. **26**: p. 88.

[5] Abrahamson, J., Wiles, P.G., and Rhoades, B.L., *Structure of carbon fibres found on carbon arc anodes.* 14th Biennial Conference on Carbon.Penn. State Univ., University Park, Penn., USA, 1979: p. 254.

[6] Nauk, I.A., *Polymeric metal complex catalysts in hydrogenation of nitrobenzene.* Metal, 1982. **3**: p. 690.

[7] Tennent, H.G., *Carbon fibrils, method for producing same and compositions containing same* 1987. **US4663230**.

[8] Wang, S., *Functionalization of Carbon Nanotubes: Characteriztion, Modeling and Composite Applications.* Ph.D. dissertation, The Florida State University, 2006.

[9] Graugnard, E., *Preliminary Examination.* Dept. of Physics, Pudue University, 1999.

[10] Qian, C., Qi, C. H., Gao, B., Cheng, Y., Qiu, Q., Qin, L. C., Zhou, O., and Liu, J., *Fabrication of small diameter few-walled carbon nanotubes with enhanced field emission property.* Journal of Nanoscience and Nanotechnology, 2006. **6**: p. 1346.

[11] Sattler, K., *Scanning tunneling microscopy of carbon nanotubes and nanocones.* Carbon, 1995. **33**: p. 915.

[12] Dresselhaus, M.S., Dresselhaus, G., and Eklund, P.C., *Science of Fullerenes and Carbon Nanotubes.* Academic Press, New York,, 1996.

[13] Ebbesen, T.W., *Carbon nanotubes.* Annual Review of Materials Science, 1994. **24**: p. 235.

[14] Dekker, C., *Carbon nanotubes as molecular quantum wires.* Physics Today, 1999. **52(5)**: p. 22.

[15] Yao, Z., Wang, J. S., Li, B., and Liu, G. R., *Thermal conduction of carbon nanotubes using molecular dynamics.* Physical review. B, 2005. **71**: p. 085417.

[16] Yi, W., L. Lu, L., Pan, Z. W., and Xie, S. S. , *Linear specific heat of carbon nanotubes.* Physical review. B, 1999. **59**: p. R9015.

[17] Cahill, D.G., Ford, W. K., Goodson, K. E., Mahan, G. D., Majumdar, A., Maris, H. J., Merlin, R., and Phillpot, S. R., *Nanoscale thermal transport.* Journal of Applied Physics, 2003. **93**: p. 793.

[18] Chiu, H.Y., Deshpande, V. V., Postma, H. W., Lau, C. N., Mik´o, C., Forr´o, L., and Bockrath, M., *Ballistic phonon thermal transport in multiwalled carbon nanotubes.* Physical Review Letters, 2005. **95**: p. 226101.

[19] Brown, E., Hao, L., Gallop, J. C., and Macfarlane, J. C., *Ballistic thermal and electrical conductance measurements on individual multiwall carbon nanotubes.* Applied Physics Letters, 2005. **87**: p. 023107.

[20] Mingo, N., Stewart, D. A., Broido, D. A., and Srivastava, D., *Phonon transmission through defects in carbon nanotubes from first principles.* Physical Review B, 2008. **77**: p.

033418.

[21] Dresselhaus, M.S., Dresselhaus, G., and Avouris, P., , *Carbon Nanotubes, Synthesis, Structure, Properties and Applications.* Springer, Berlin, 2001.

[22] Chang, C.W., Okawa, D., Majumdar, A., and Zettl, A., *Solid-State Thermal Rectifier.* Science, 2006. **314**: p. 1121.

[23] Kim, P., Lieber, C. M., *Nanotube Nanotweezers.* Science, 1999. **286**: p. 2148.

[24] Gao, B., Bower, C., Lorentzen, J. D., Fleming, L., Kleinhammes, A., Tang, X. P., McNeil, L. E., Wu, Y., and Zhou, O., *Enhanced saturation lithium composition in ball-milled single-walled carbon nanotubes.* Chemical Physics Letters, 2000. **327**: p. 69.

[25] Kong, J., Franklin, N. R., Zhou, C., Chapline, M. G., Peng, S., Cho, K., and Dai, D., *Nanotube Molecular Wires as Chemical Sensors.* Science, 2000. **287**: p. 622.

[26] Wang, Q.H., Yan, M., and Chang, R. P. H. , *Flat panel display prototype using gated carbon nanotube field emitters.* Applied Physics Letters, 2001. **78**: p. 1294.

[27] Tans, S.J., Verschueren, A. R. M., and Dekker, C., *Room temperature transistor based on a single carbon nanotube.* Nature, 1998. **393**: p. 49

[28] Martel, R., Derycke, V., Lavoie, C., Appenzeller, J., Chan, K. K., Tersoff, J., and Avouris, P., *Ambipolar Electrical Transport in Semiconducting Single-Wall Carbon Nanotubes.* Physical Review Letters, 2001. **87**: p. 256805.

[29] Radosavljevic, M., Appenzeller, J., Avouris, P., and Knoch, J., *High performance of potassium ndoped carbon nanotube field-effect transistors.* Applied Physics Letters, 2004. **84**: p. 3693.

[30] Neophytou, N., Kienle, D., Polizzi, E., and Anantram, M. P., *Influence of defects on nanotube transistor performance.* Applied Physics Letters 2006. **88**: p. 242106.

[31] Jun, L., Ng, H. T., Cassell, A., Fan, W., Hua Chen, Ye, Q., Koehne, J., Han, J., and

Meyyappan, M., *Carbon Nanotube Nanoelectrode Array for Ultrasensitive DNA Detection.* Nano Letters, 2003. **3**(5): p. 597.

[32] Mendoza, E., Henley, S. J., Poa, C. H. P., Chen, G. Y., Giusca, C. E., Adikaari, A.A.D.T., Carey, J. D., and Silva, S. R. P. , *Large area growth of carbon nanotube arrays for sensing platforms.* Sensors and Actuators B, 2005: p. 75.

[33] Sun, L., Banhart, F., Krasheninnikov, A. V., Rodríguez-Manzo, J. A., Terrones, M. and Ajayan, P. M., *Carbon Nanotubes as High-Pressure Cylinders and Nanoextruders.* Science, 2006. **312**: p. 1199.

[34] Vinayak, P., *Controlled-Size Nanocapsules.* Nature, 1995. **374**: p. 602.

[35] Britto, P.J., Santhanam, K. S. V., and Ajayan, P. M., *Carbon nanotube electrode for oxidation of dopamine.* Bioelectrochemistry and Bioenergetics, 1996. **41**: p. 121.

[36] Binnig, G., Quate, C. F., and Gerber, C., *Atomic Force Microscope.* Phys. Rev. Lett. , 1986. **56**: p. 930.

[37] Wiesendanger, R., *Scanning probe microscopy and spectroscopy, Methods and applications.* Cambridge University Press, Cambridge, Great Britain, 1994.

[38] Giessibl, F.J., *Advances in atomic force microscopy.* Rev. Mod. Phys. , 2003. **75**: p. 949.

[39] *Digital Instruments, V.M.G., Scanning Probe Microscopy Training Notebook. http://www.eng.yale.edu/uelm/Document%5Cafm.pdf, 2000.*

[40] Ghafari, P., St-Denis, C. H., Power, M. E., Jin, X., Tsou, V., Mandal, H. S., Bols, N. C., and Tang, X.,, *Impact of carbon nanotubes on the ingestion and digestion of bacteria by ciliated protozoa.* Nature Nanotechnology, 2008. **3**: p. 347.

[41] Kurt, R., Klinke, C., Bonard, J. M., Kern, K., and Karimi, A., *Tayloring the diameter of decorated C-N nanotubes by temperature variations using HF-CVD.* Carbon, 2001. **39**: p. 2163.

[42] Tuinstra, F., Koenig, J. L., *Raman spectrum of graphite.* J. Chem. Phys., 1970. **53**: p. 1126.

[43] Dillon, R.O., Woollam, J. A., and Katkanant, V., *Use of Raman-scattering to investigate disorder and crystallite formation in as-deposited and annealed carbon-films.* Phys. Rev. B, 1984. **29**: p. 3482.

[44] Iijima, S., *Helical Microtubules of Graphitic Carbon.* Nature, 1991. **354**: p. 56.

[45] Guo, T., Nikolaev, P., Rinzler, A. G., Tomanek, D., Colbert, D. T., and Smalley, R. E. , *Self assembly of tubular fullerenes.* J. Phys. Chem, 1995. **99**(10): p. 694.

[46] Kong, J., Soh, H. T., Cassell, A. M., Quate, C. F., and Dai, H., *Synthesis of Individual Single-Walled Carbon Nanotubes on Patterned Silicon Wafers.* Nature, 1998. **878**: p. 6705.

[47] Li, Y., Mann, D., Rolandi, M., Kim, W., Ural, A., Hung, S., Javey, A., Cao, J., and Wang, D. and Q.W. E. Yenilmez, J. F. Gibbons, Y. Nishi, and H. Dai, H. , *Preferential growth of semiconducting single-walled carbon nanotubes grown by Plasma enhanced CVD method,.* Nano Letters, 2004. **4**: p. 317.

[48] Kanzow, H., Schmalz, A., and Ding, A.,, *Laser-assisted production of multi-walled carbon nanotubes from acetylene.* Chem. Phys. Lett., 1998. **295**: p. 525.

[49] ShiMuchi, H., Ohno, Y., Kishimoto, S., and Mizutani, T., *Suppression of hysteresis in carbon nanotube field-effect transistors :Effect of contamination induced by device fabrication process.* Japanese Journal of Applied physics, 2006. **45**: p. 5501.

[50] Roertson, D.H., Brenner, D.W. , *Mintminre, Energetics of nanoscale graphitic tubules.* .W. Phys. Tev.B, 1992. **45**: p. 12592.

[51] Eanes E. D., P., A. S., *Meeting of the Division of Biophysics, Trans. N. Y. Acad. Sci.* 1965. **28**: p. 233.

[52] Sun, S., Murray, C. B.,Weller, D., Folks, L., and Moser, A., *Monodisperse FePt nanoparticles and ferromagnetic FePt nanocrystal superlattices.* Science, 2000. **287**: p. 1989.

[53] Smith, T.W., Wychlck, D. J., *Preparation of Monodispersed Fe-Mo Nanopaticles as the Catalyst for CVD Synthesis of Carbon nanotubes.* Phys. Chem., 1980. **84**: p. 1621.

[54] Mannistu K. D., Y.H.W., and Masliyah J. H., *Solubility Modeling of Asphaltenes in Organic Solvents.* Energy Fuels, 1997. **11**(3): p. 615.

[55] Raty, J., Gygi, F., and Galli, G., *Growth of Carbon Nanotubes on Metal Nanoparticles: A Microscopic Mechanism from Ab Initio Molecular Dynamics Simulations.* Physical Review Letters, 2005. **95**: p. 096103.

[56] Harutyunyana, A.R., Tokune, T., Mora, E., Bolton, K., and Curtarolo, S., *"Building" the catalyst for the Growth of Single-Walled Carbon Nanotubes.* Journal of Applied Physics, 2006. **100**: p. 044321.

[57] Lammert, P.E., Zhang, P., and Crespi, V. H., *Gapping by Squashing: Metal-Insulator and Insulator-Metal Transitions in Collapsed Carbon Nanotubes.* Phys. ReV. Lett. , 2000. **84**: p. 2453.

[58] Liang, W., Cheung, C.-L., Lieber, C. M., and Park, H. , *Unpublished results.*

[59] Dai, H., Wong, E. W., Lu, Y. Z., Fan, S. S., and Lieber, C. M. , *Synthesis and characterization of carbide nanorods.* Nature, 1995. **375**: p. 769.

[60] Schlesinger, M., Paunovic, M. (editors), *Modern Electroplating (4th edition), Wiley, New York.* Wiley, New York, 2000.

[61] Paunovic, M., and Schlesinger, M., *Fundamentals of Electrochemical Deposition.* Wiley, New York, 1998.

[62]. Bobo, J.F., Gabillet, L., and Bibes, M., *Interaction effects in magnetic oxide*

nanoparticle systems. J. Phys.: Condens. Matter, 2004. **16**: p. s471.

[63] Sun, S., Murray, C. B.,Weller, D., Folks, L., and Moser, A., *Monodisperse FePt nanoparticles and ferromagnetic FePt nanocrystal superlattices.* Science, 2000. **287**: p. 1989.

[64] Tartaj, P., Morales, M. P., Veintemillas-Verdaguer, S., González-Carreño, T., and Serna, C. J., *The Preparation of Magnetic Nanoparticles for Applications in Biomedicine.* J. Phys.D: Appl. Phys., 2003. **36**: p. 182.

[65] Sun, Y.G., and Xia, Y. N., *Shape-Controlled Synthesis of Gold and Silver Nanoparticles* Science, 2002. **298**: p. 2176.

[66] Zhang, H.R., Shen, C. M., Chen, S. T., Xu, Z. C., Liu, F. S., Li, J. Q., and Gao, H. J., *Morphologies and microstructures of nano-sized Cu2O particles using a cetyltrimethylammonium template.* Nanotechnology, 2005. **16**: p. 267.

[67] Avouris, P., *Molecular electronics with carbon nanotubes.* Acc. Chem. Res. , 2002. **35**: p. 1026.

[68] Krupke, R., Hennrich, F., Lohneysen, H., and Kappes, M. M., *Electronic and Optical Properties of Molecular Nanostructures* Science, 2003. **301**: p. 344.

[69] Li, Y., *Preferential Growth of Semiconducting Single-Walled Carbon Nanotubes by a Plasma Enhanced CVD Method.* Nano Lett. , 2004. **4**: p. 317.

[70] Seidel, R.V., Graham, A.P., Rajasekharan, E., Unger,E., Liebau, M., Duesberg, D.S., Kreupl, F., Hoenlein, W., *Bias dependence and electrical breakdown of small diamete single-walled carbon nanotubes.* J.Appl.Phys., 2004. **96**: p. 66949. 71.

[71]. Javey, A., Guo, J., Paulsson, M., Wang, Q., Mann, D., Lundstrom, M., and Dai, H. J., *High- field quasiballistic transport in short cabon nanotubes.* Phys.Rev.Lett., 2004. **92**: p. 106804.

[72] Pop, E., Mann, D., Goodson, K., and Dai, H., *Electrical and thermal transport in metallic single-wall carbon nanotubes on insulating substrates.* J. Appl. Phys., 2007. **101**: p. 093710.

[73] Hata, K., Futaba, D. N., Mizuno, K., Namai, T.,Yumura, M., and Iijima, S., *Water-assisted highly efficient synthesis of impurity-free single-walled carbon nanotubes.* Science, 2004. **306**: p. 1362.

[74] Chiang, I.W., Brinson, B. E., Huang, A. Y., Willis, P. A., Bronikowski, M. L., Margrave, J. L., Smalley, R. E., and Hauge, R. H., *Purification and characterization of single-wall carbon nanotubes (SWNTs) obtained from the gas-phase decomposition of CO (HiPco process).* J. Phys. Chem. B, 2001. **105**: p. 8297.

[75] Radushkevich, L.V., Lukyanovich, V. M., *O strukture ugleroda, obrazujucegosja pri termiceskom azlozenii okisi ugleroda na zeleznom kontakte.* Zurn Fisic Chim, 1952. **26**: p. 88.

[76] Ouyang, Y., and Guo, J., *Heat dissipation in carbon nanotube transistors* Applied Physics Letters, 2006. **89**: p. 183122.

[77] Bachtold, A., Hadley, P., Nakanishi, T., and Dekker, C., *Logic Circuits with Carbon Nanotube Transistors* Science, 2001. **294**: p. 1317.

[78] Palacios, J.J., *First principles phase-coherent transport in metallic nanotubes with realistic contacts.* Phys. Rev. Lett., 2003. **90**: p. 106801.

[79] Frank, S., Poncharal, P., Wang, Z. L., and De Heer, W. A., *Carbon Nanotube Quantum Resistors* Science, 1998. **280**: p. 1744.

[80] Collins, P.G., Arnold, M. S., and Avouris, P.. *Engineering Carbon Nanotubes and Nanotube Circuits Using Electrical Breakdown.* Science, 2001. **292**: p. 706.

[81] Collins, P.G., Hersam, H., Arnold, M., Martel, R., and Avouris, P., *Current saturation*

and electrical breakdown in multiwalled carbon nanotubes. physical Review Letters, 2001. **86**: p. 3128.

[82] Bachtold, A., Strunk, C., Salvetat, J-P., Bonard, J-M., Forro, L., Nussbaumer, T., and Schenenberger, C., *Aharonov-Bohm oscillations in carbon nanotubes.* Nature, 1999. **397**: p. 673.

[83] Jang, W.Y., Kulkarni, N. N., Shih, C. K., and Yao, Z., *Effect of Bi surfactant on atomic ordering of GaAsSb.* Applied Physics Letters, 2004. **84**: p. 1177.

[84] Park, H., Lim, A. K. L., Alivosatos, A. P., Park, J., and McEuen, P. L., *Fabrication of metallic electrodes with nanometer separation by electromigration.* Applied Physics Letters, 1999. **75**: p. 301.

[85] Fujii, A., Tsutsui, M., Kurokawa, S., and Sakai, A., *Break conductance of noble metal contacts.* physical Review B, 2005. **72**: p. 045407.

[86] Thelander, C., and Samuelson, L., *AFM manipulation of carbon nanotubes: realization of ultra-fine nanoelectrodes.* Nanotechnology, 2002. **13**: p. 108.

[87] Jung, T.A., Schlitter, R. R., Gimzewski, J. K., Tang, H. and Joachim, C. , *Controlled Room-Temperature Positioning of Individual Molecules: Molecular Flexure and Motion* Science, 1996. **271**: p. 181.

[88] Lefebvre, J., Lynch, J. F., Llaguno, M., Radosavljevic, M., and Johnson, A. T., *Single-wall carbon nanotube circuits assembled with an atomic force microscope.* Applied Physics Letters, 1999. **75**: p. 3014.

[80] Yao, Z., Postma, H. W. C., Balents, L., and Dekker, C, *Carbon nanotube intramolecular junctions.* Nature, 1999. **402**: p. 273.

[90] Postma, H.W.C., Jonge, M., Yao, Z., and Dekker, C., *Electrical transport through*

carbon nanotube junctions created by mechanical manipulation. Physical Review B, 2000. **62**: p. R10653.